

6. Meteorological Phenomena

6.1. Heavy Rain Associated with the Baiu Front

The Baiu front has a small horizontal temperature gradient but a large horizontal water vapor gradient, accompanied by a strong low-level jet and an intense inflow of warm wet air (known as “moist tongue”). East-west cloud bands corresponding to the front in satellite imagery are a rich source of information on such bands (widths, lengths, meridional displacement, and convective clouds within them) and convective clouds entering cloud bands (development and movement) to indicate frontal activity. Satellite imagery-based monitoring of heavy rain associated with the front is important because it enables visualization of dry intrusion, upper vortices and movement of active convective clouds.

In this section, the characteristics of satellite imagery for the Baiu front are described in relation to a case (20 – 21 June 2016) in which conditions were simultaneously affected by an upper trough and warm wet air. Rainfall exceeding as much as 100 mm per hour was recorded in the prefectures of Kumamoto and Nagasaki. In particular, precipitation of 150 mm per hour was recorded in Kosa-machi, Kumamoto, which was unprecedented locally and the fourth-highest ever in the whole of Japan at the time.

(1) Baiu Front Cloud Band and Warm Sector Convective Cloud Area

Outline

When the upper trough approaches the cloud band corresponding to the front, a bulging cloud area begins to form with anticyclonic curvature at its northern edge. In the lower layer on the warm side, a warm air mass with high specific humidity moves north toward the cloud band along the western edge of the Pacific High. Convective cloud lines can be seen among the warm air masses.

Analysis

1. Upper vortex corresponding to the trough and bulging cloud areas

As the upper trough approaches, a thick bulging cloud area begins to form as also seen in the formative and development stages of cyclones. The upper trough in water vapor imagery corresponds closely to the upper vortex.

In this case, water vapor image shows a trough axis between the Bohai Sea and the Yellow Sea (Fig. 6-1-1). Another trough in association with a dry area in the middle layer over western Kyushu is also seen. These characteristics correspond to positive vorticity maximum areas on the 500 hPa vorticity analysis chart (A and B in Fig. 6-1-2). In infrared imagery (Fig. 6-1-3), active cumulonimbus clouds are seen to the front of the trough around Kyushu. Bulging cloud expansion is also seen at the northern edge of the cloud band between western Japan and the western part of the Sea of Japan.

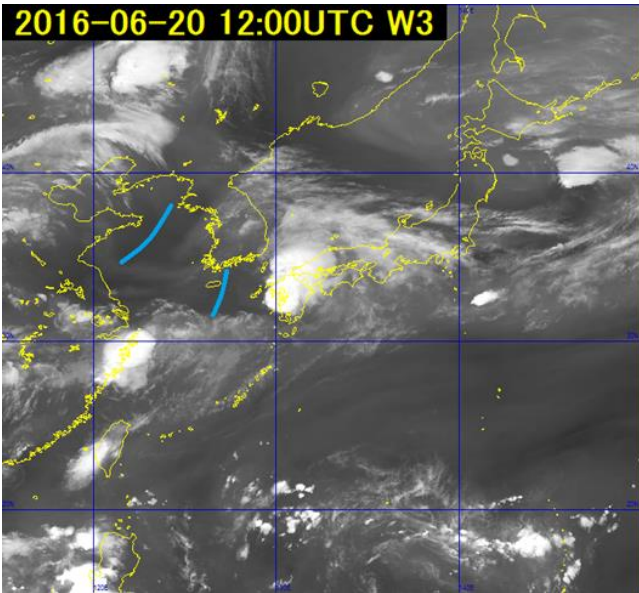


Fig. 6-1-1 B10 water vapor image for 12:00 UTC on 20 June 2016

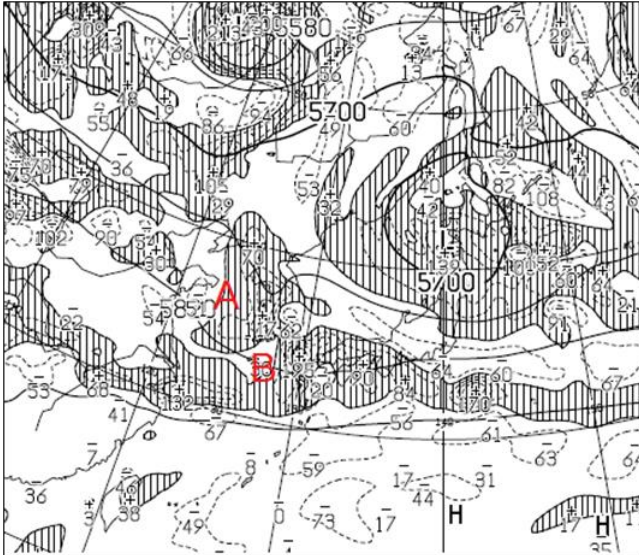


Fig. 6-1-2 500 hPa vorticity analysis chart or 12:00 UTC on 20 June 2016

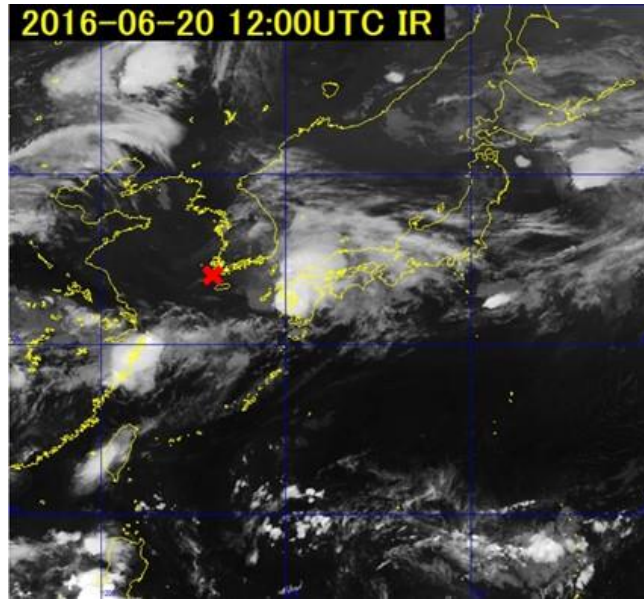


Fig. 6-1-3 B13 infrared image for 12:00 UTC on 20 June 2016

X marks the lower vortex

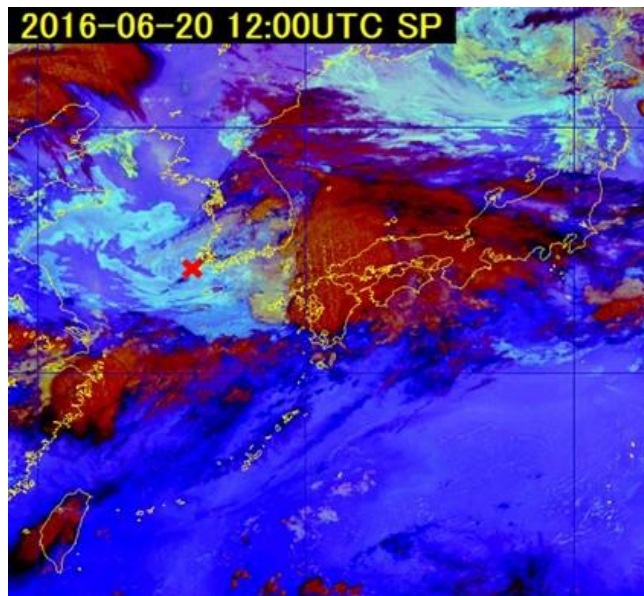


Fig. 6-1-4 Night Microphysics RGB composite image, for 12:00 UTC on 20 June 2016

X marks the lower vortex.

2. Areas of active convection near the front and in the warm sector

Active convective cloud areas and cloud lines often correspond to wind convergence areas and high equivalent-potential temperature zones in the lower layer.

In this example (Figs. 6-1-3 and 6-1-4), B13 infrared image and Night Microphysics RGB composite image reveal a lower vortex corresponding to a cyclone below the trough over the northwestern part of Jeju Island, with a front corresponding to the northern edge of the bulging Ci discussed above. The Cb area around Kyushu is associated with the eastern part of the dark region, with multiple carrot-shaped precipitation zones as seen in Fig. 6-1-5, moving

slowly eastward along with the movement in the same direction of the dark region of the trough at 500 hPa as discussed above. Night Microphysics RGB composite imagery shows scattered low-level clouds moving northward toward the frontal cloud band.

Figure 6-1-6 shows Airmass RGB composite image with 925 hPa equivalent potential temperature (reddish purple) and winds (green barbs) based on JMA's mesoscale numerical weather prediction model (MSM). Here, warm moist air with high equivalent-potential temperature flowed from the southwest toward Kyushu. Northeast of the Cb area, strong velocity convergence is seen. In the same area, the horizontal gradient of equivalent potential temperature is large and winds are orthogonal to the isometric lines of equivalent potential temperature, indicating that the northeastern part of the Cb area has the largest advection. Southwestern winds of 50 kt are observed in western Kyushu, and wind profiler data from Kumamoto shows similar winds at an altitude of 500 m from around 14:00 UTC onward (figure not shown).

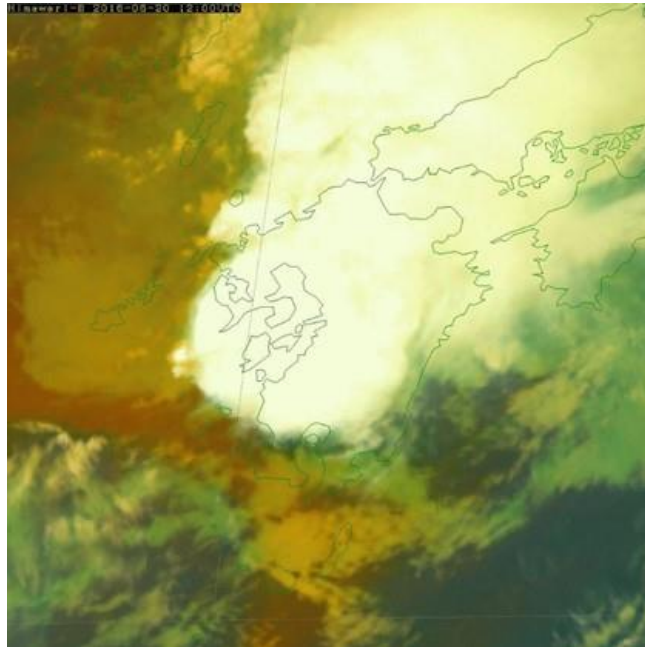


Fig. 6-1-5 Airmass RGB composite image for 12:00 UTC on 20 June 2016

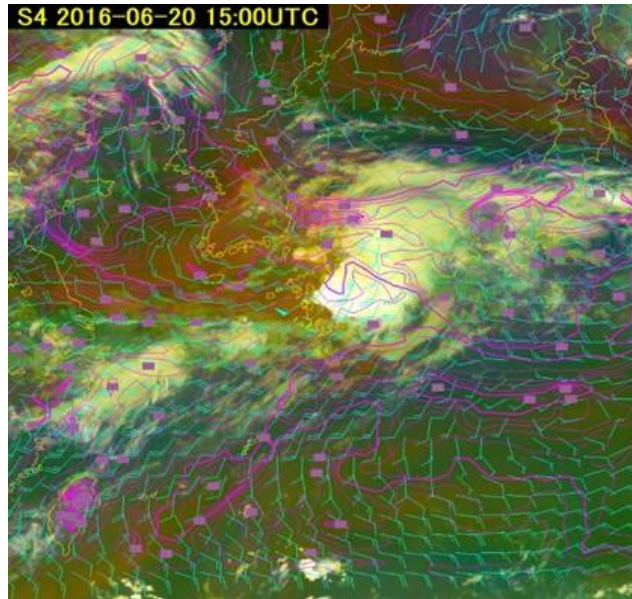


Fig. 6-1-6 Airmass RGB composite image for 15:00 UTC on 20 June 2016
925 hPa equivalent potential temperature (reddish purple) and winds (green barbs) based on
MSM objective analysis with temporally corresponding initial values.

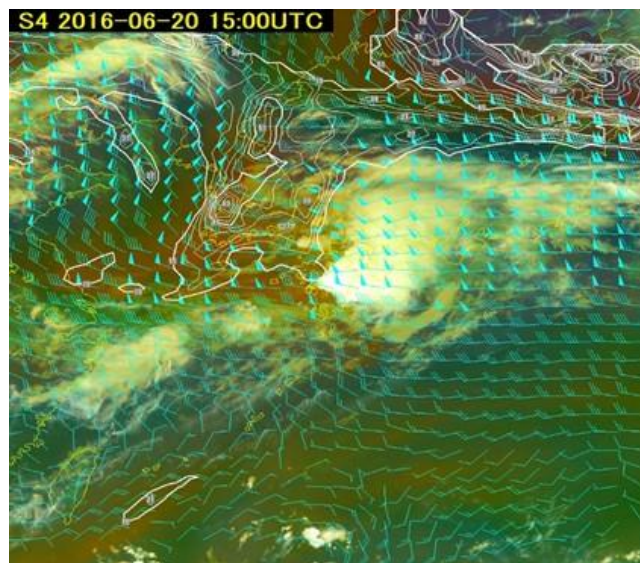


Fig. 6-1-7 Airmass RGB composite image for 15:00 UTC on 20 June 2016
250 hPa winds (green barbs) and potential vorticity at the 345 K isentropic surface (dark red)
based on MSM objective analysis with temporally corresponding initial values.

3. Entrance of high potential vorticity and upper divergence

Figure 6-1-7 shows Airmass RGB composite image with potential vorticity at the 345 K isentropic surface and 250 hPa winds.

Wind distribution shows intense horizontal divergence around the Cb, as seen with the formation conditions for carrot-shaped Cb, indicating strong divergence in the upper layer. In potential vorticity distribution, a high potential-vorticity area above 1.5 PVU spreads from north to south with convective clouds ahead, as seen in the dry area of the dark region in the

upper and middle layers corresponding to the brown area in Airmass RGB composite imagery. In the advection area with high potential vorticity, updraft is promoted from the middle layer to the upper layer (Japan Meteorological Agency, 2013).

As described in 2 and 3, carrot-shaped Cb areas were formed in association with strong advection near the front in the lower layer and strong divergence in the upper layer.

(2) Summary

1. Key points in relation to heavy rainfall brought by the Baiu front

A) Updraft causing convective clouds

Lower-layer convergence ahead of cyclones, intensification of equivalent potential temperature advection near the front, and orographic effects

B) Atmospheric structures promoting convective cloud development

Low-level advection of high equivalent-potential temperature, dry intrusion from the north of the front (i.e., convective instability), intrusion of cold air (i.e., latent instability), and divergence in the upper layer

C) Sufficient water vapor supply

Intrusion of air parcels with high specific humidity toward the front

D) Synoptic field conditions for maintenance of the above

Positioning of jets/troughs/cyclones, presence of tropical disturbances over the sea south of Japan, and subtropical anticyclone intensity

2. Baiu-Front characteristics relating to heavy rainfall

A) A bulging thick cloud area forms in the cloud band corresponding to the front as the upper trough approaches.

B) In areas with lower-layer convergence, convection becomes active and cloud bands corresponding to the front are formed.

C) In warm areas, convection becomes active in high equivalent-potential temperature zones in the lower layer in association with Pacific High marginal winds.

D) In areas with strong warm humid advection brought by marginal winds, convection becomes active at the southern edge of the cloud band.

References:

- Japan Meteorological Agency (2013) Weather Forecast Training Textbook (in Japanese).

6.2. Heavy Snow Associated with a Small Cyclone on the Western Coast of Hokkaido

In winter, a trough forms as a result of a relatively warm area over the sea to the west of Hokkaido surrounded by two cold anticyclones, one is above Primorye in Russia, and the other is above Sakhalin, Hokkaido, and ice on the Sea of Okhotsk. This leads to the latitudinal formation of a convergence line between the Strait of Tartary and the northern Sea of Japan associated with seasonal northwest wind and northeast winds blowing from the cold anticyclone above Sakhalin, Hokkaido, and ice on the Sea of Okhotsk. An updraft occurs along this line, and belt-form clouds emerge as a result (Fig. 6-2-1). When the upper trough and the area with maximum positive vorticity approach the belt-form clouds, updraft intensifies to bring a lower vortex containing convective clouds. A small cyclone and a bag-shaped low-pressure area are subsequently analyzed.

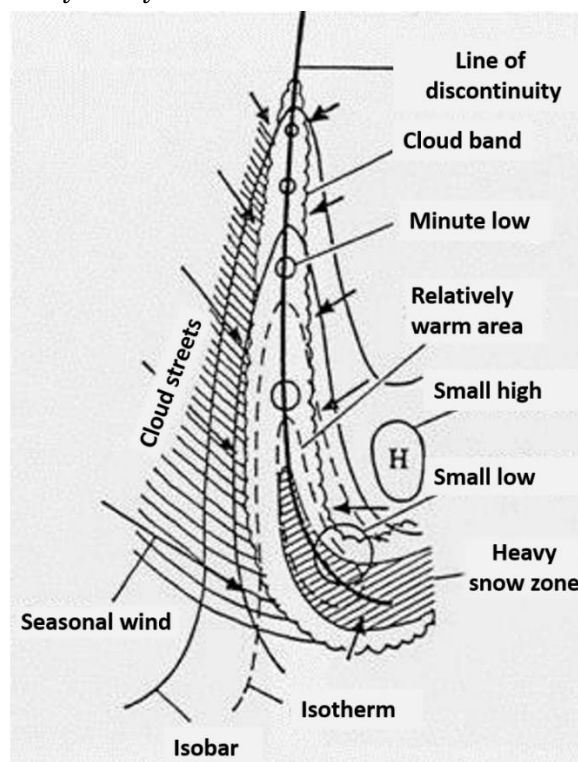


Fig. 6-2-1 Cloud bands on the western coast of Hokkaido (Okabayashi, 1972). Arrows: lower winds; thick solid line: convergence; area inside wavy line: cloud band; thin solid lines: isobars; dashed lines: ground-level isotherms.

Hokkaido Western Coast Small Lows are a type of mesoscale lower vortex. Among these are Ishikari Bay Lows, in which the vortex moves southward with winds, often bringing heavy snow to western Hokkaido. In previous research, the Sapporo District Meteorological Observatory extensively surveyed Hokkaido Western Coast Small Lows (Sapporo District Meteorological Observatory, 1989). In this study, clouds are classified into two patterns (belt or vortex form) and seven genres based on characteristics seen in satellite imagery, with the creation of a cloud formation flowchart and a worksheet for forecasting snowstorms with each

cloud type. In this section, a Hokkaido Western Coast Small Low is described on the basis of satellite imagery.

(1) Characteristics Seen in Satellite Imagery

Around 14:00 UTC on 13 January 2016, two mesoscale lower vortices emerged over the northern Sea of Japan and developed rapidly off the shores of Rumoi and the Shakotan Peninsula under the influence of an upper trough moving along the polar-front jet stream. These vortices and a surrounding spiral-form Cb area subsequently moved southeastward and landed in the subprefectures of Rumoi and Shiribeshi, bringing heavy snowfall to the latter.

1 Before lower-vortex emergence

In the surface weather chart for 12:00 UTC on 13 January 2016, a cyclone was advancing eastward from the western part of the Tsugaru Strait before lower-vortex emergence (Fig. 6-2-2). In the 500 hPa upper weather chart, an upper trough with a cold-air mass below -42°C was advancing toward Primorye (Fig. 6-2-3). Infrared image shows belt-form convective clouds over the sea off western Hokkaido (Fig. 6-2-4, with a thin solid line connecting active convective clouds in the belt-form convective cloud area, forming the curve marked as **E1**).

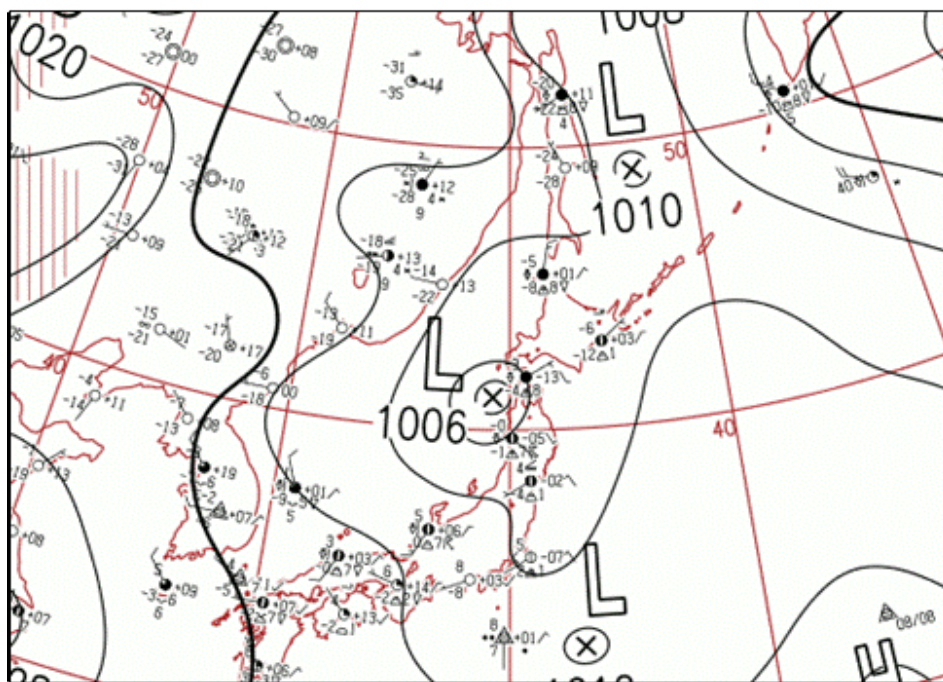


Fig. 6-2-2 Surface weather chart for 12:00 UTC on 13 January 2016

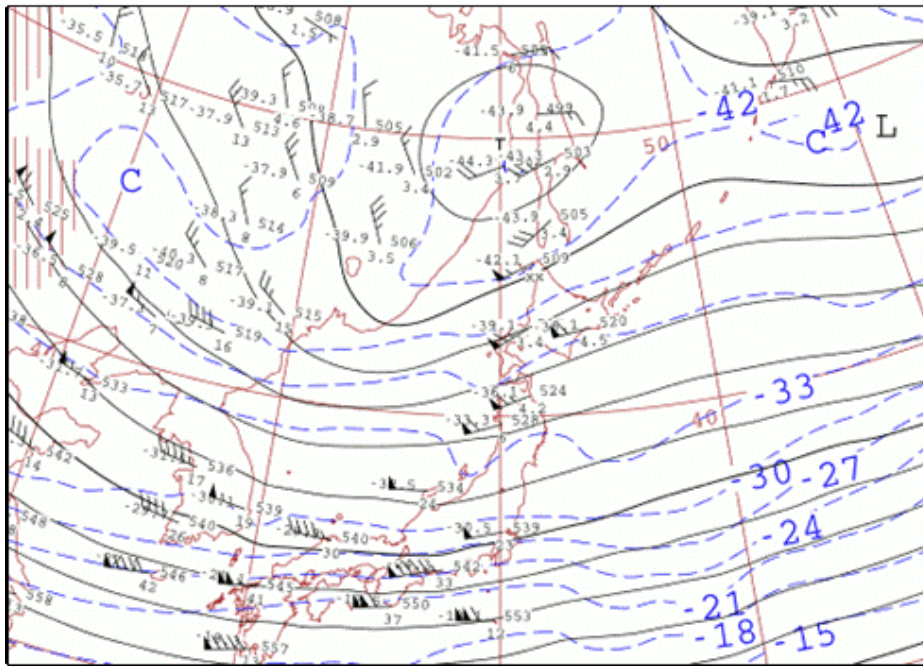


Fig. 6-2-3 500 hPa upper weather chart for 12:00 UTC on 13 January 2016

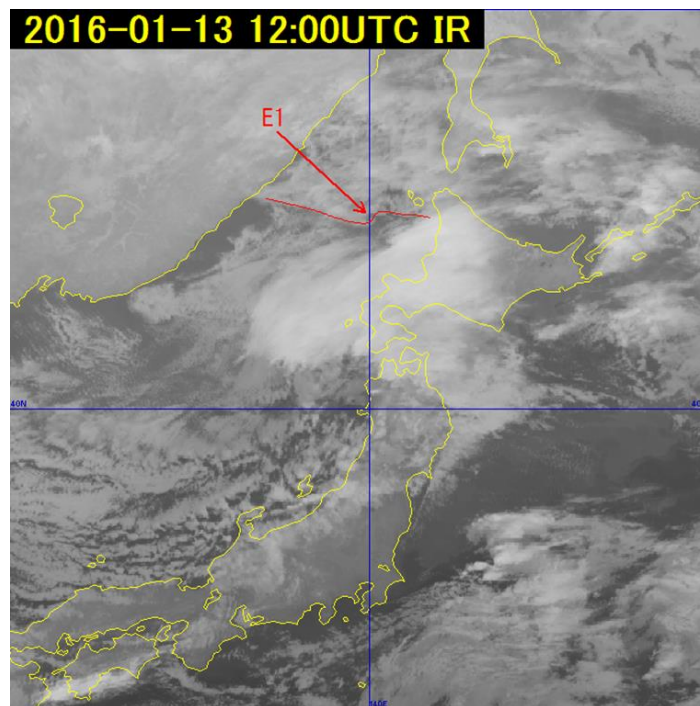


Fig. 6-2-4 B13 infrared image for 12:00 UTC on 13 January 2016

2 Lower-vortex formative stage

In the surface weather chart for 18:00 UTC on 13 January 2016, a cyclone was advancing off the coast of Hidaka, bringing the typical “west-high, east-low” pressure pattern seen in Japan in winter (Fig. 6-2-5). In infrared image, belt-form convective clouds were moving southward with increasing activity, and the curve **E1** was moving east-southeastward, overlapping with upper clouds and becoming obscure (Fig. 6-2-6). The upper trough at 500 hPa was progressing

east-northeastward producing a distinct bulging cloud formation over the sea off western Hokkaido in front of the trough, along with the emergence of the mesoscale lower vortex **E2** to its west.

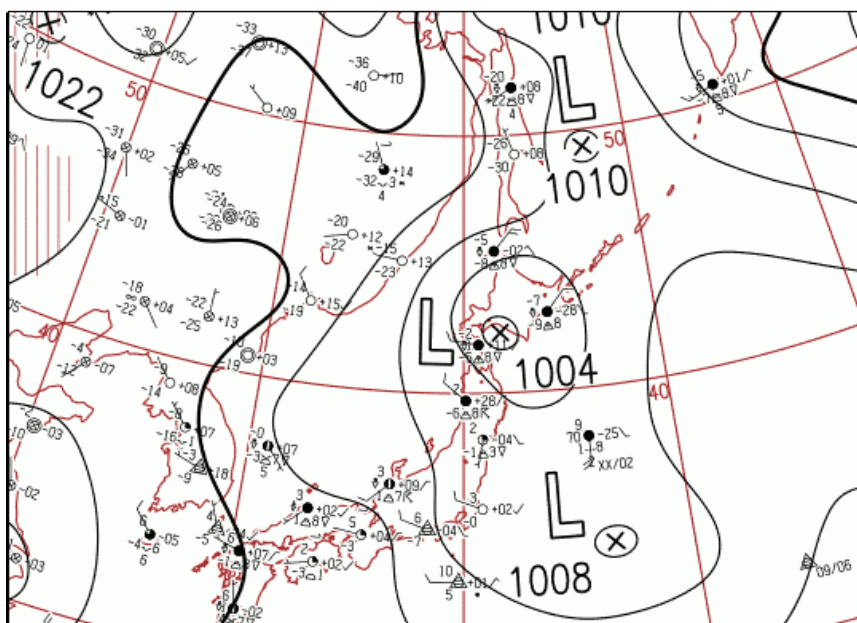


Fig. 6-2-5 Surface weather chart for 18:00 UTC on 13 January 2016

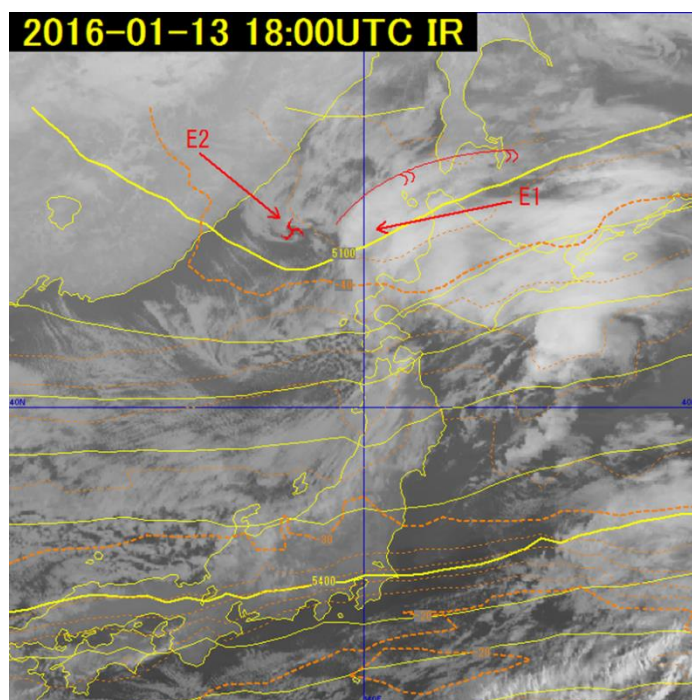


Fig. 6-2-6 B13 infrared image for 18:00 UTC on 13 January 2016, with 500 hPa geopotential heights and temperatures based on MSM objective analysis with temporally corresponding initial values

3 Lower-vortex development stage

In the infrared image for 21:00 UTC on 13 January 2016, upper clouds over the sea off western Hokkaido were advancing east-northeastward, and curve **E1** was moving onto the

upper trough at 500 hPa, forming a distinctive mesoscale lower vortex off the shore of Rumoi (Fig. 6-2-7). A spiral-form Cb area was seen around the lower vortex, and radar echo intensity increased.

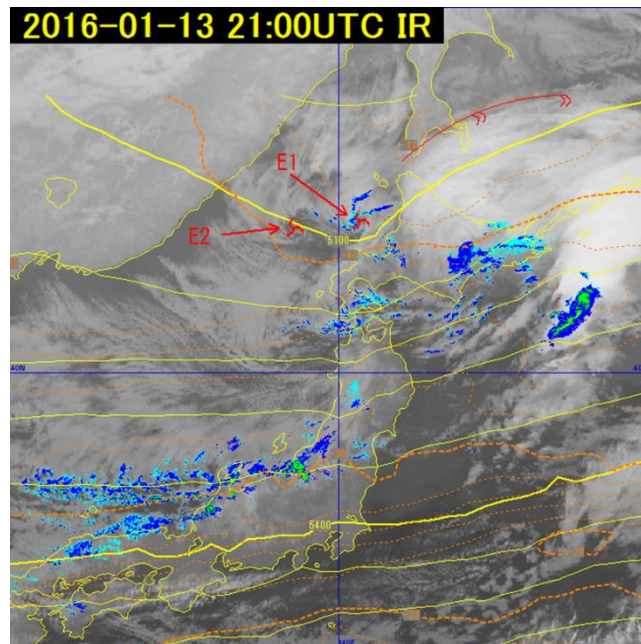


Fig. 6-2-7 B13 infrared image for 21:00 UTC on 13 January 2016, with 500 hPa geopotential heights and temperatures based on MSM objective analysis with temporally corresponding initial values and radar echoes

4 Lower-vortex mature stage

In infrared image for 00:00 UTC on 14 January 2016, the lower vortices **E1** and **E2** were accompanied by a distinct spiral-form Cb area and advancing east-southeastward while maintaining high levels of convective activity (Figs. 6-2-8, 6-2-9). **E1** is accompanied by a Cb area with a minimum brightness temperature of around -33°C and a maximum cloud top height of approximately 4,000 m, or 600 hPa (Fig. 6-2-10).

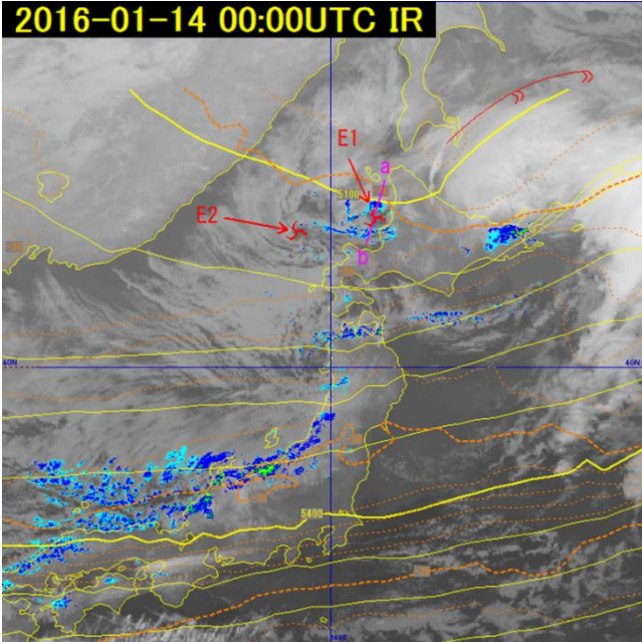


Fig. 6-2-8 B13 infrared image for 00:00 UTC on 14 January 2016, 500 hPa geopotential heights and temperatures by MSM objective analysis with temporally corresponding initial values, and radar echoes

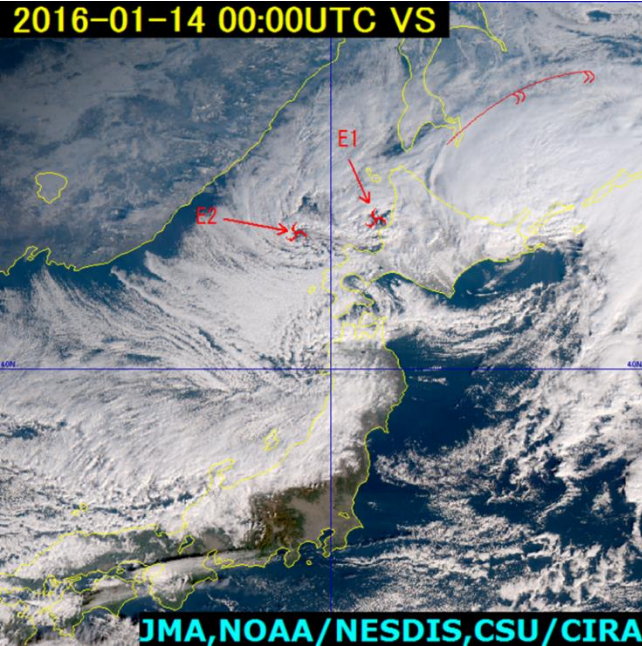


Fig. 6-2-9 True Color Reproduction image for 00:00 UTC on 14 January 2016

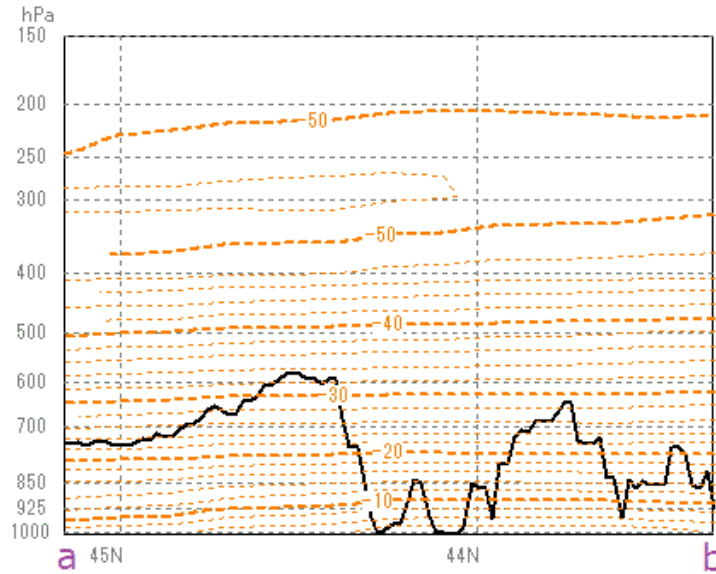


Fig. 6-2-10 Vertical cross section between a and b in Figure 6-2-8. Dashed orange lines are isotherms and the black line is cloud top height distribution. Both from MSM objective analysis with initial values at 00:00 UTC on 14 January 2016.

5 Lower-vortex dissipation stage

In the infrared image for 06:00 UTC on 14 January 2016, the lower vortex **E1** has landed near Rumoi and weakened along with its surrounding convective clouds (Fig. 6-2-11). The lower vortex **E2** has become obscure off the shore of the Shakotan Peninsula, and another mesoscale lower vortex **E3** has appeared. It is surrounded by a spiral-form Cb area, and has advanced east-southeastward and moved over an area near the Shakotan Peninsula (Fig. 6-2-12).

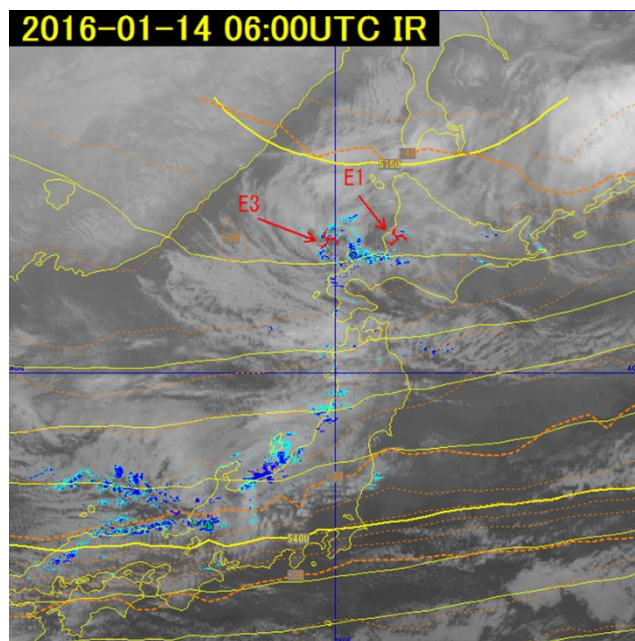


Fig. 6-2-11 B13 infrared image for 06:00 UTC on 14 January 2016, with 500 hPa

geopotential heights and temperatures based on MSM objective analysis with temporally corresponding initial values and radar echoes

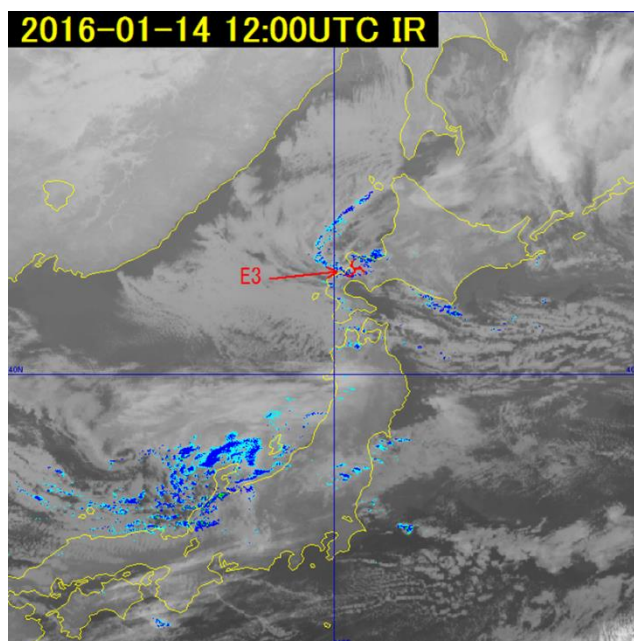


Fig. 6-2-12 B13 infrared image with radar echoes for 12:00 UTC on 14 January 2016

Figure 6-2-13 shows time-series graphs of snowfall observed by AMeDAS (JMA's Automated Meteorological Data Acquisition System consisting of automated weather stations) in Kutchan and Kimobetsu in Shiribeshi Subprefecture. At both sites, heavy snowfall was recorded approximately between 07:00 and 13:00 UTC. As in this example, mesoscale cloud vortices and cloud bands emerging over the northern Sea of Japan can bring heavy snowfall upon landing. Accordingly, it is necessary to monitor mesoscale disturbances and accompanying active convective clouds through satellite image (Fig. 6-2-14).

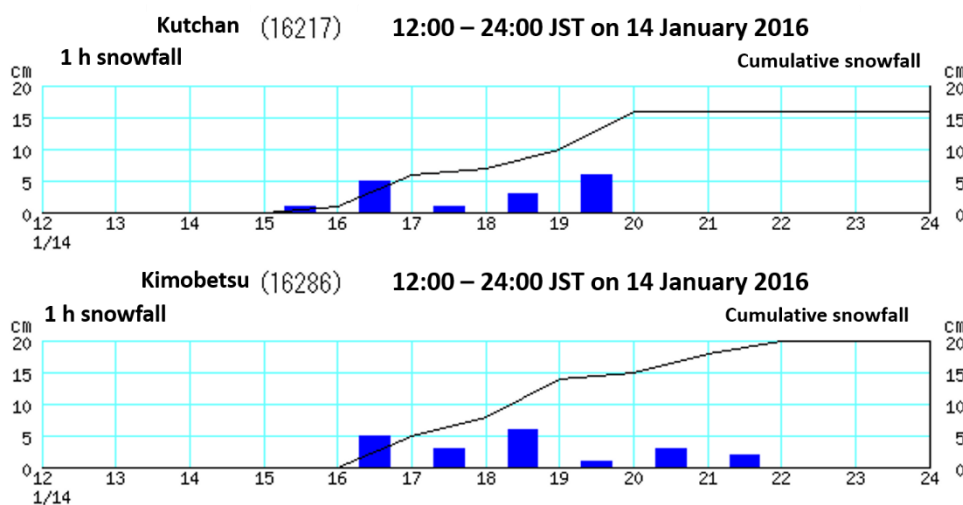


Fig. 6-2-13 Time-series graphs of snowfall observed by AMeDAS in Kutchan and Kimobetsu

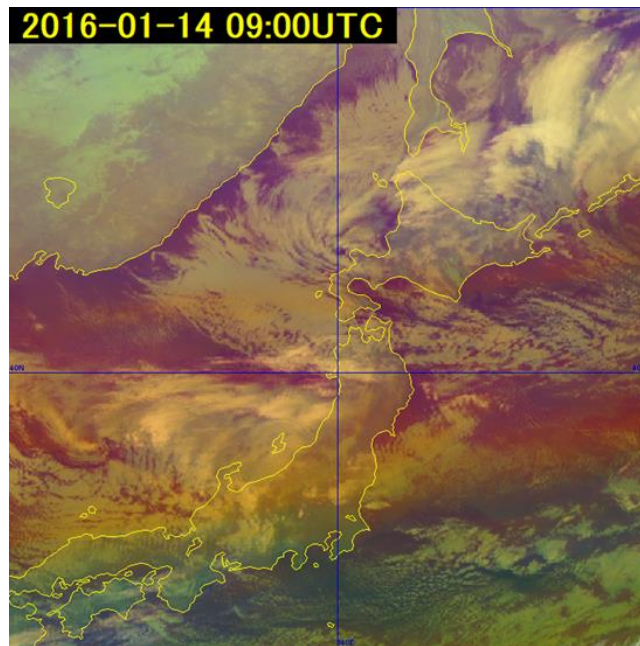


Fig. 6-2-14 Airmass RGB composite image for 09:00 UTC on 14 January 2016

(2) Typical Winter Pressure Patterns in Japan

Japan's typical winter "west-high, east-low" pressure pattern is associated with cold dry anticyclones in Siberia and cyclones in eastern Japan. Northwest seasonal winds running from high- to low-pressure areas pick up sensible heat and water vapor from the warm surface of the Sea of Japan, generating cloud streets and bringing snowfall along the mountains on the country's Sea of Japan side (known as mountain-type snowfall). However, heavy snowfall may also affect coasts and plains (plain-type snowfall). This section outlines the relationship between cloud street strikes, snowfall distribution, surface isobars and wind direction at 850 hPa.

Although a number of other elements contribute to snowfall (e.g., intensity and movement of cold-air masses at 500 hPa) focus here is placed on cloud street strikes for their visibility in satellite image.

1. Mountain-type heavy snowfall on 20 January 2016

In this event, a trough was present to the east of Hokkaido and a large zonal pressure gradient was observed over the northern Sea of Japan. The center of an upper cold-air mass with prominent lower cold advection was present over northern Japan. This pressure pattern tends to produce north-to-south cloud street strikes over the Sea of Japan, leading to strong northwest seasonal winds. Cb clouds develop on the windward side of Japan's backbone mountains, bringing heavy snow (Fig. 6-2-15). Snowfall with this pattern generally occurs from the Hokuriku region to the San'in region.

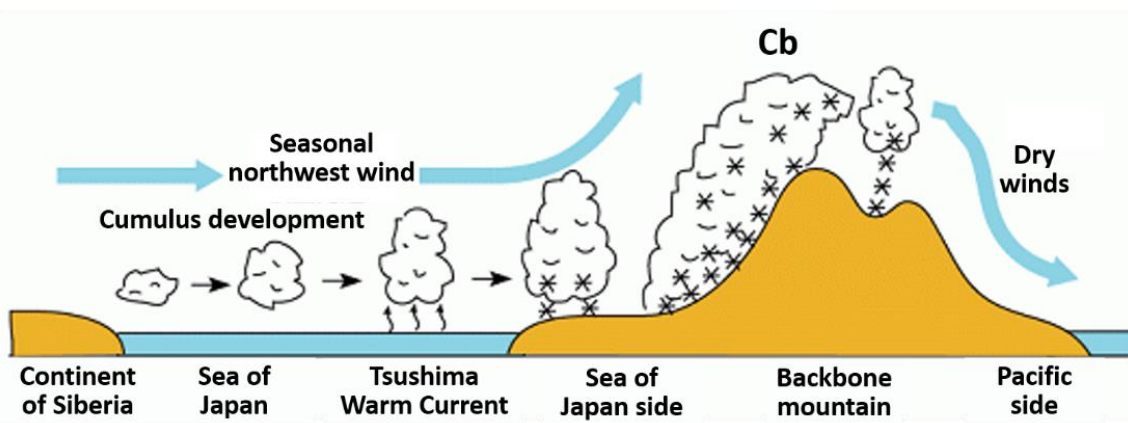


Fig. 6-2-15 Schematic drawing of mountain-type snowfall
(from the homepage of Matsue Local Meteorological Office)

A cyclone over the central Sea of Japan at 00:00 UTC on 19 January had advanced to sea areas near the Kuril Islands by 00:00 UTC on 20 January, and the zonal pressure gradient increased. Isobars around Japan became nearly meridional (Fig. 6-2-16). The cloud street strike direction generally matched the wind direction at 850 hPa (Fig. 6-2-17).

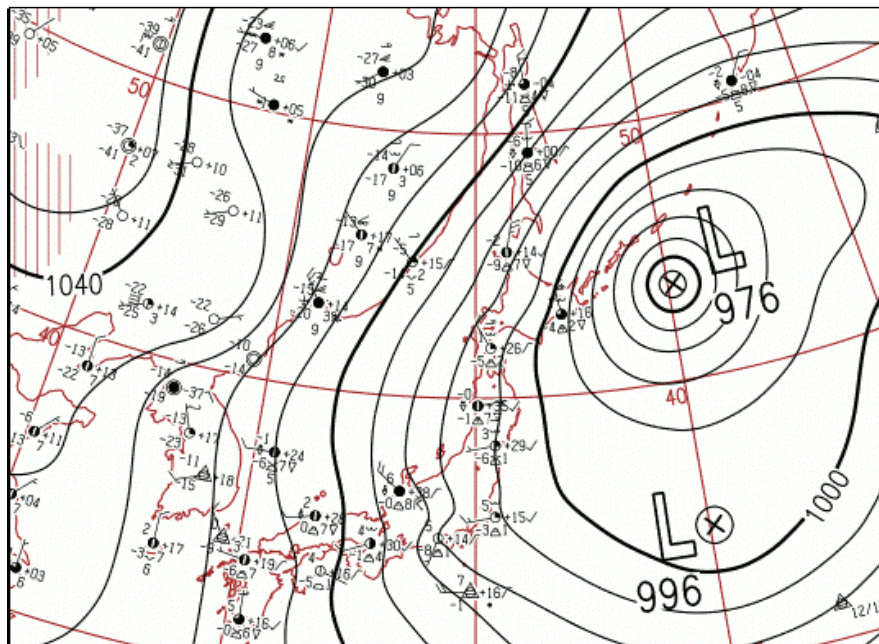


Fig. 6-2-16 Surface weather chart for 00:00 UTC on 20 January 2016

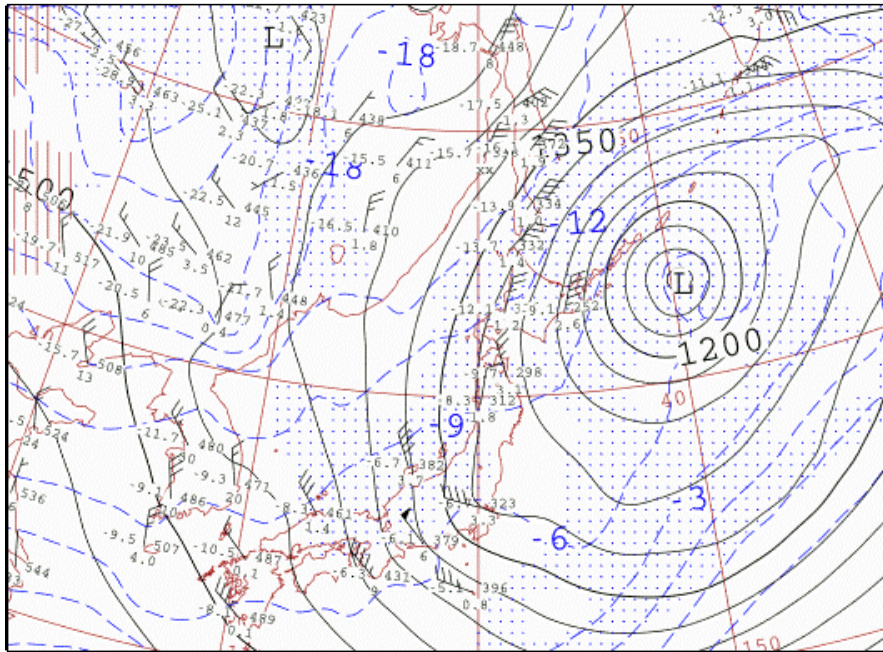


Fig. 6-2-17 850 hPa upper weather chart for 00:00 UTC on 20 January 2016

In infrared image for 00:00 UTC on 20 January, cloud streets containing Cb were observed over the Sea of Japan, and tall cloud streets that had passed over Sekigahara, the Kii Channel and the Bungo Channel were seen on the Pacific side. In the 24 hours until 15:00 UTC on 20 January, heavy snowfall of 42 cm in Sugadaira, Nagano Prefecture, and 41 cm in Kusatsu, Gunma Prefecture was recorded (Fig. 6-2-19).

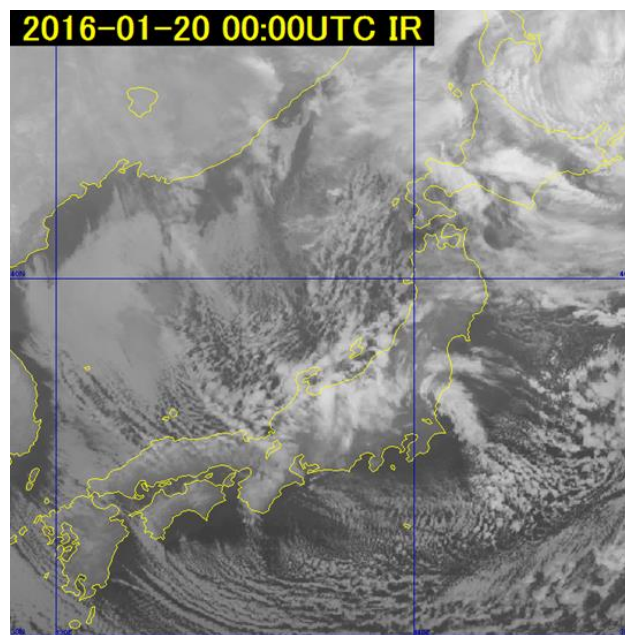


Fig. 6-2-18 B13 infrared image for 00:00 UTC on 20 January 2016

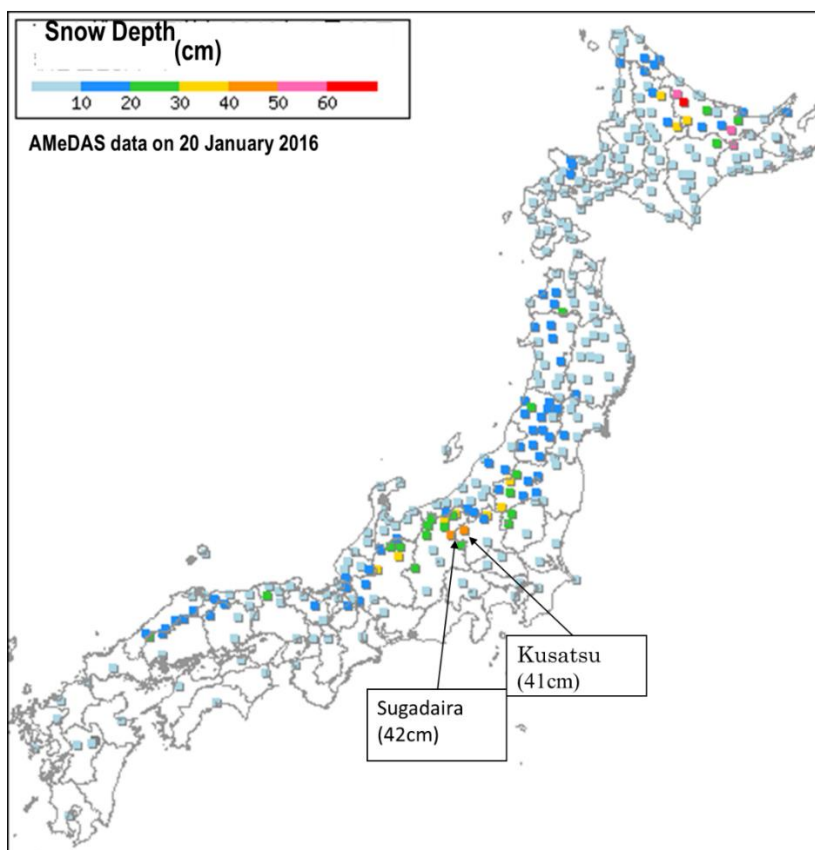


Fig. 6-2-19 Distribution of 24-hour snowfall observed by AMeDAS

2 Plain-type heavy snowfall on 16 February 2016

In this example, the center of an upper cold air mass was present over the western Sea of Japan, the zonal pressure gradient was relatively gentle over the Sea of Japan in general, and seasonal surface winds were relatively weak. With this pattern, the cloud street strike direction is often from west to east. Convective instability may increase, and minor cyclones on the ground may arise when an upper cold low moves toward the Sea of Japan. As a result, Cb clouds develop and move over Japan, and heavy snowfall is observed in coastal and plain areas (Fig. 6-2-20). Snowfall associated with this pattern generally occurs on the Sea of Japan side of the area from the Tohoku region to the Hokuriku region.

A cyclone over the northern Sea of Japan at 00:00 UTC on 15 February approached the Kuril Islands at 00:00 UTC on 16 February, and an anticyclone over the continent began expanding eastward from South China, resulting in the typical winter pressure pattern seen around Japan with a trough over the western Sea of Japan (Fig. 6-2-21). The isobars over the northern Sea of Japan struck from northwest to southeast. The pressure gradient weakened over the central and western Sea of Japan, resulting in isobars with a zonal direction.

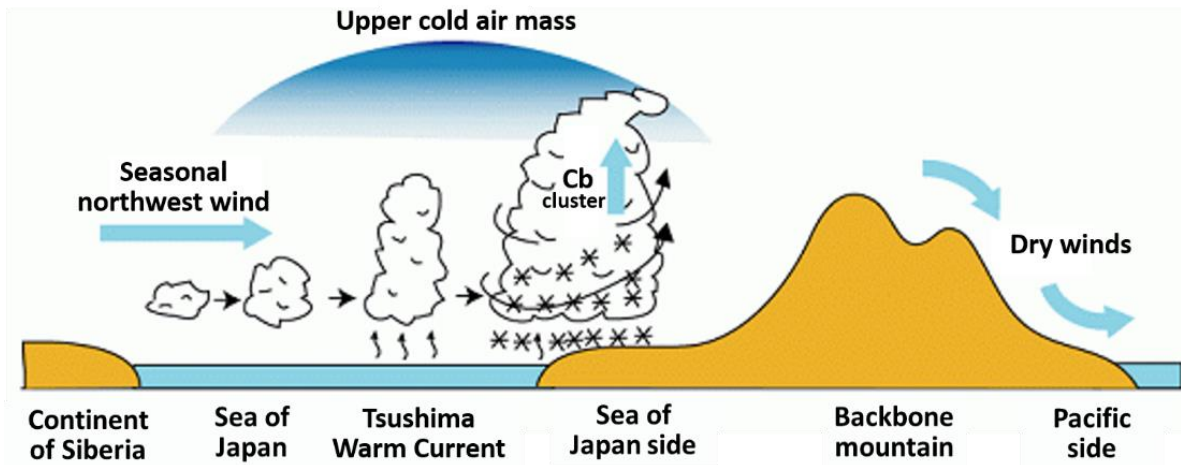


Fig. 6-2-20 Schematic drawing of plain-type snowfall
(from the homepage of Matsue Local Meteorological Office)

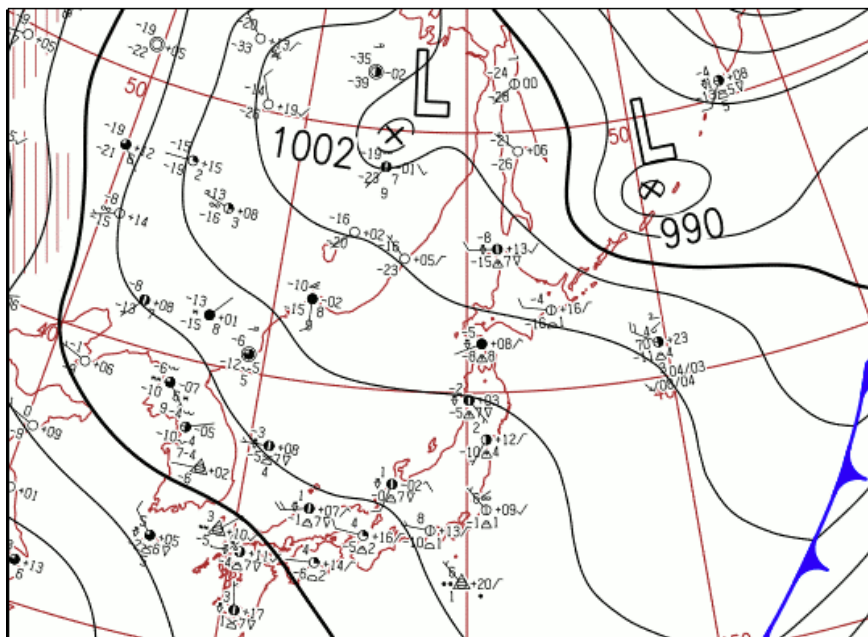


Fig. 6-2-21 Surface weather chart for 00:00 UTC on 16 February 2016

In infrared image for 00:00 UTC on 16 February, cloud streets with east-west strikes were seen over the western Sea of Japan, almost parallel to the isobars and the wind direction seen at 850 hPa (Fig. 6-2-22). Cu and some Cg were observed, and heavy snowfall occurred in overcast areas from the Noto Peninsula to the Tohoku region along the Sea of Japan.

In the 24 hours until 15:00 UTC on 16 February, heavy snowfall was observed in Oisawa, Yamagata Prefecture (35 cm) and Yashima, Akita Prefecture (32 cm) (Fig. 6-2-24).

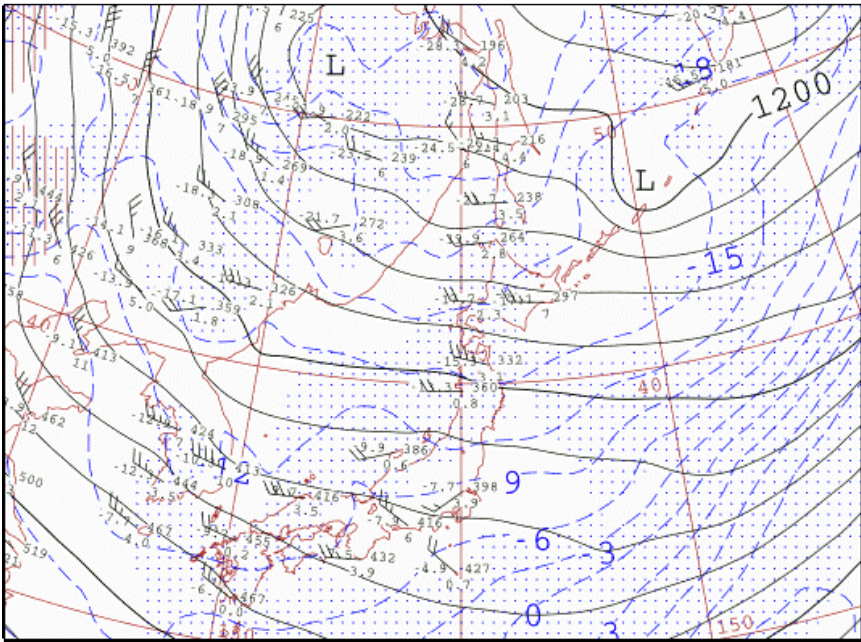


Fig. 6-2-22 850 hPa upper weather chart for 00:00 UTC 16 February 2016

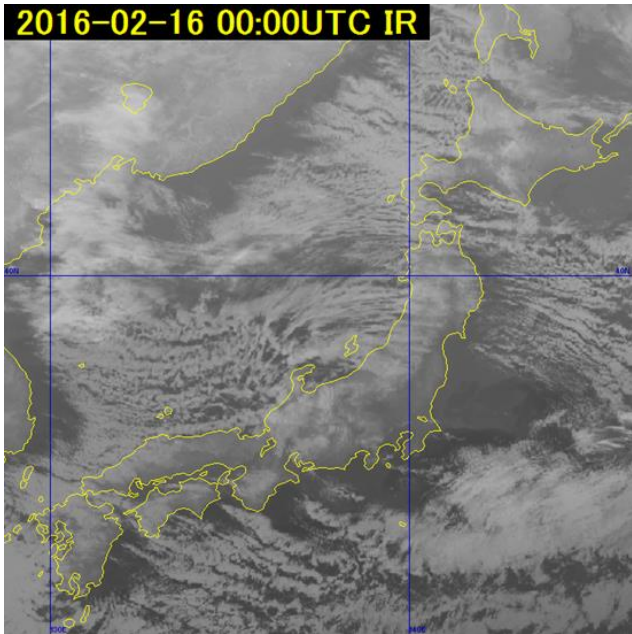


Fig. 6-2-23 B13 infrared image for 00:00 UTC 16 February 2016

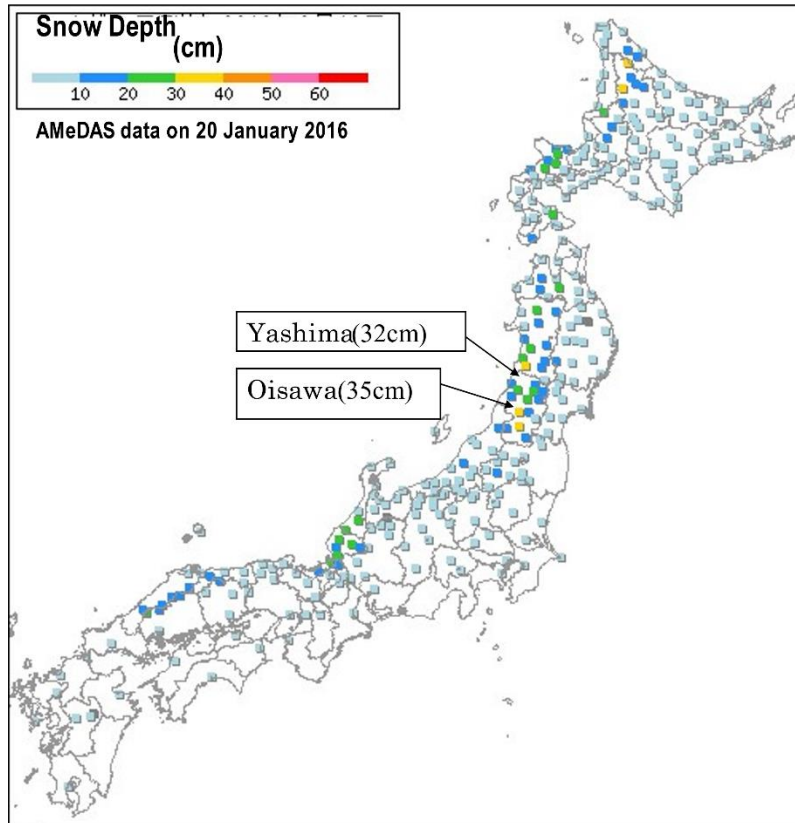


Fig. 6-2-24 Distribution of 24-hour snowfall observed by AMeDAS

References:

- Okabayashi, T. (1972) Snow Clouds seen from Satellite and their Use in Study on Snowfall, *Kisyo-kenkyu Note*, 113, 74-106. (In Japanese)
- Sapporo District Meteorological Observatory (1989) Study on Small Low generating around Western Coast of Hokkaido, *Technical Report of Sapporo District Meteorological Observatory (Special issue 38)*, 137 pp. (In Japanese)

6.3. Strong Winds

Obtaining wind information from satellite data generally involves calculating motion by tracking cloud cells in successive images. In some cases, characteristic cloud patterns emerge with strong winds (“Surface wind speeds exceed 20 kt when convective cloud lines composed of cloud streets form along cold air mass blowout”; Meteorological Satellite Department, 1976), and “Wind speeds exceed 20 kt at mountain tops when lee wave clouds emerge on their lee side. The interval between associated cloud streets is proportional to the wind speed, and the interval widens as wind speed increases; Obana, 1983”.

This section presents extraction of information on lower winds based on the passage of a cold front in winter.

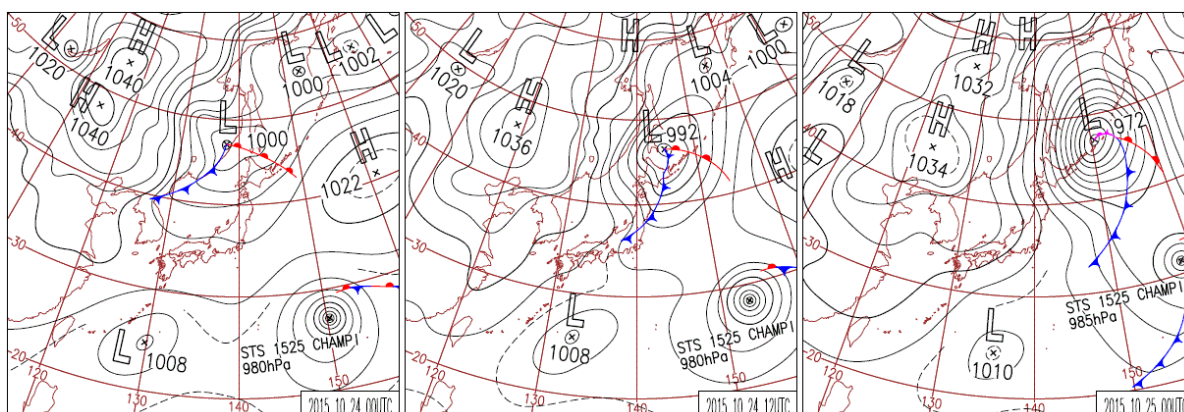


Fig. 6-3-1 Surface weather charts

Left: for 00:00 UTC on 24 October 2015, center: for 12:00 UTC on 24th, right: for 00:00 UTC on 25th

6.3.1. Strong Winds When a Cold Front Passes

Between 24 and 25 October 2015, a cyclone developed rapidly near Primorye, Russia, characterized by a central pressure reduction of 28 hPa by the time of its passage over northern Hokkaido. A winter-type pressure pattern formed around Japan, and north-northwest winds with maximum instantaneous speeds of 13.3 m/s were recorded at 02:54 UTC (11:54 JST) on 24 October in Tokyo.

(1) When the Cold Front is over the Sea of Japan

In the surface weather chart for 00:00 UTC on 24 October, a low pressure area is seen around Primorye, and the cold front is located around the northern part of the Korean Peninsula (Fig. 6-3-1). The cloud area corresponding to the cold front has not been organized, and no corresponding cloud area is seen in satellite imagery (figure not shown).

Focus here is placed on the cold front along the Sea of Japan. Figure 6-3-2 shows infrared image from nine hours after the above situation. The cloud area corresponding to the cold front is distinct, and can be inferred as an **A-B** Cb-Cu line extending from Akita Prefecture to offshore San'in. This line advanced east-southeastward or southeastward at speeds of 30 – 35

kt. Convective cloud streets accompanying the cold-air mass were as yet indistinct over the central Sea of Japan to the rear of the front, but were visible over the sea's northern part.

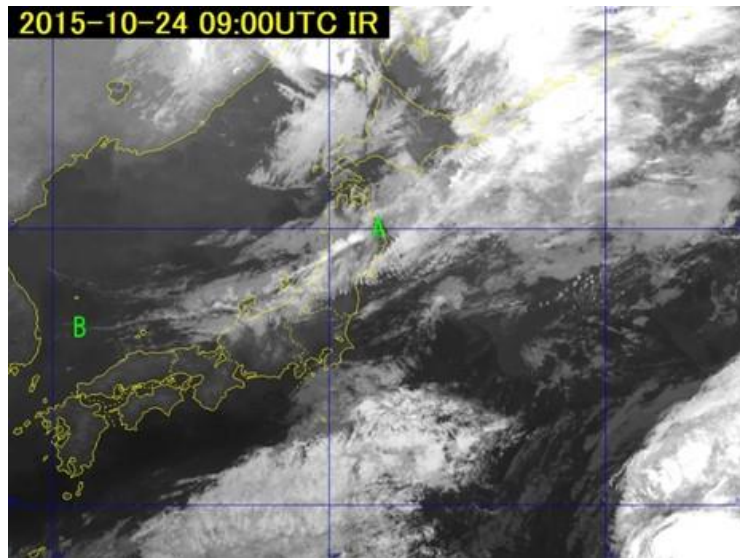


Fig. 6-3-2 B13 infrared image for 09:00 UTC on 24 October 2015

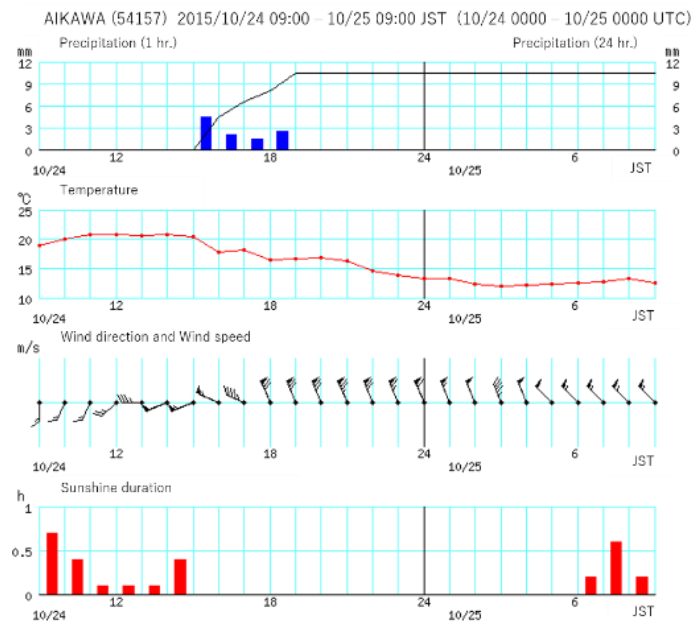


Fig. 6-3-3 Time-series graph of AMeDAS observations in Aikawa, Niigata Prefecture, between 00:00 UTC (09:00 JST) on 24 and 00:00 UTC (09:00 JST) on 25 October 2015

Strong winds with directions between west-northwest and northwest at the rear of the cold front can be inferred from the movement of the Cb-Cu line. Figure 6-3-3 shows the following:

1. The wind direction changed from west-southwest to west-northwest, and temperatures declined around 07:00 UTC (16:00 JST).
2. The wind direction changed from west-northwest to north-northwest, the wind speed increased, and the temperature declined around 09:00 UTC (18:00 JST).

The maximum instantaneous wind speed of 20.8 m/s (40 kt; north-northwest) was observed at 08:48 UTC (17:48 JST), indicating that the latter change corresponds to the Cb-Cu line in the satellite image. The maximum wind speed of 15.9 m/s (31 kt; north-northwest) was observed at 11:28 UTC (20:28 JST), which closely correlates with the movement speed (30 – 35 kt) of the **A-B** Cb-Cu line.

(2) When the Cold Front is Inland

When passing over the backbone mountains, the Cb-Cu line became obscure, making it difficult to locate the front over the inland area in satellite image. Here, the time at which the front passed over the Kanto region is estimated from time-series AMeDAS observations in Tokyo as shown in Fig. 6-3-4. A change in wind direction from west-southwest to west-northwest is seen at 12:30 UTC (21:30 JST) on 24 October. Wind speeds showed a decreasing tendency after the wind direction changed to west-northwest, but increased from 0.4 m/s (1 kt) at 13:50 UTC (22:50 JST) to 9.2 m/s (18 kt) at 15:10 UTC (00:10 JST on the 25th). The temperature showed a gradually decreasing tendency overnight, with no obvious change associated with the passage of the front. These observations suggest that the cold front passed over Tokyo at around 12:30 UTC (21:30 JST) on 24 October. In this example, there was a time lag of 2 – 3 hours until winds strengthened after the front's passage.

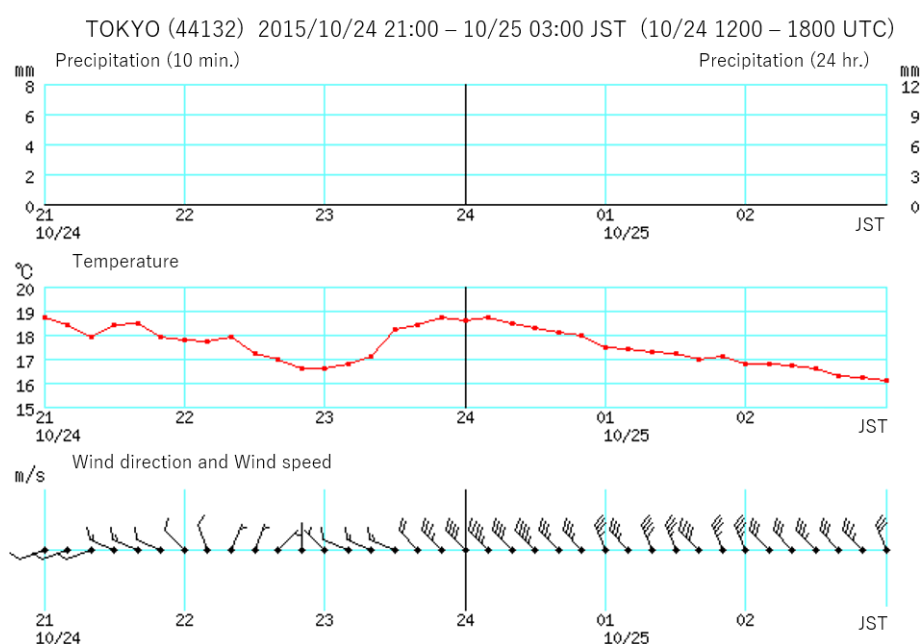


Fig. 6-3-4 Time-series graph of AMeDAS observations in Tokyo between 12:00 UTC (21:00 JST) and 18:00 UTC (03:00 JST on the next day) on 24 October 2015

The infrared image in Fig. 6-3-5 shows characteristics present just before the cold front passed. Some convective clouds over the Sea of Japan moved over land on became obscure, but others remained over the sea and were traceable. The lines for these clouds reach the area

around A-B in the figure. Over the northern Sea of Japan, cloud streets accompanying the cold-air mass developed and expanded, indicating an inflow of cold air. Lee wave clouds are seen around Sado Island, Chubu and over the sea east of Japan, indicating strong winds in the upper atmosphere.

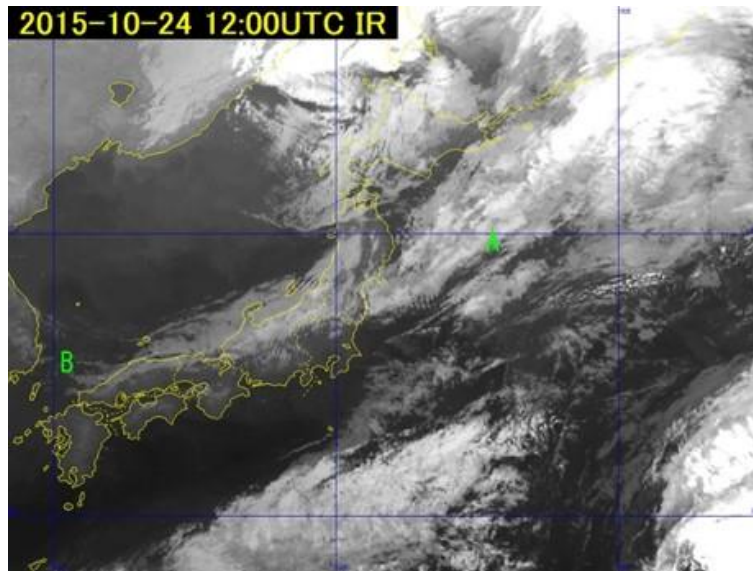


Fig. 6-3-5 B13 infrared image for 12:00 UTC on 24 October 2015

Wind speeds can be estimated from the interval between lee wave cloud lines because the two are proportional (Section 3.7 Lee Wave Clouds). In this example, the wind speed U (m/s) can be estimated using the wavelength λ (km) of the lee wave clouds emerging around Sado Island and the equation proposed by G.A. Corby (1957):

$$U = 1.7\lambda + 4.8.$$

The distance between the cloud lines in the infrared image is approximately 15 km (Fig. 6-3-6), suggesting a wind speed of 30.3 m/s (59 kt). This roughly matches the speed of 60 kt estimated from GSM data at the cloud top height (approx. 600 hPa) of the lee wave clouds in this cross-section (Fig. 6-3-7).

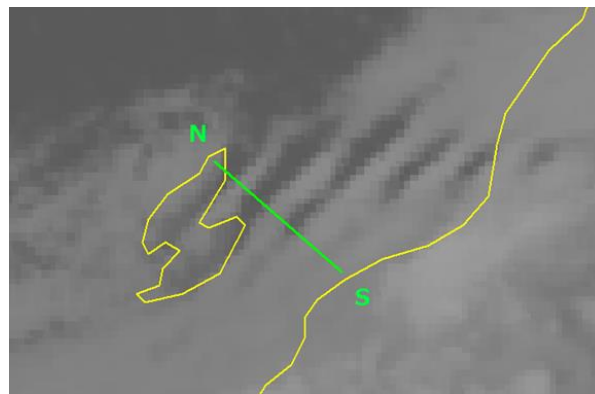


Fig. 6-3-6 B13 infrared image for 12:00 UTC on 24 October 2015

Enlarged view of the area around Sado Island. The cross-section at the green line **NS** was analyzed.

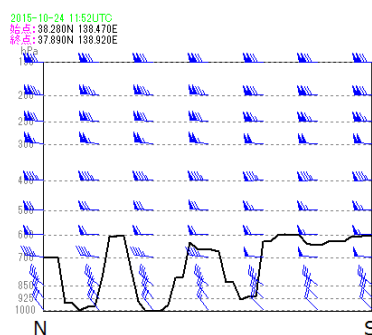


Fig. 6-3-7 Cross-section values along the line **NS** for 12:00 UTC on 24 October 2015.

Line: brightness temperature converted to pressure

Barbs: wind direction and speed (pennants: 50 kt; long barbs: 10 kt; short barbs: 5 kt). Both from GSM data

(3) When the Cold Front Passes to the Pacific

In the infrared image for 00:00 UTC on the 25th after the front passed over Japan, skies over the inland area of Kanto are clear, as commonly seen in winter, influenced by the backbone mountains (Fig. 6-3-8). Meanwhile, the Hokkaido and Tohoku regions were affected by the cold air mass and strong winds, and were covered by convective cloud streets from the Sea of Japan to the Pacific. The convective cloud cells moved at 25 – 30 kt southeastward in the area offshore of Akita on the Sea of Japan side and at 40 – 45 kt southeastward in the area offshore of Sanriku on the Pacific side. These values are in close agreement with those at 850 hPa calculated from GSM data.

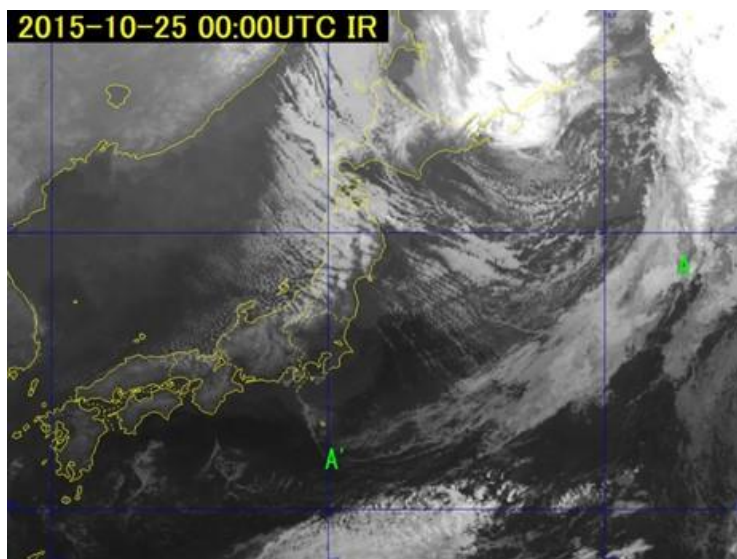


Fig. 6-3-8 B13 infrared image for 00:00 UTC on 25 October 2015

A to A' shows the position of the front from satellite imagery

6.3.2. Key points in Analyzing Strong Winds by Satellite Imagery and Its Applications

Utilization of Meteorological Satellite Data in Cloud Analysis

- (1) Cu clouds emerging with cold-air inflow begin to form streets when the surface wind speed exceeds 20 kt. Determination of the movement of individual cells in cloud streets and analysis of low-level winds allows estimation of wind speeds over land and sea. Since cloud streets strike parallel to the wind direction over land and sea, wind direction can be estimated from that (Meteorological Satellite Department, 1976).
- (2) When lee wave clouds form on the leeward side of mountain ranges, the wind speed around mountain tops is expected to exceed 20 kt. As intervals between lee wave cloud lines exhibits a linear relationship with wind speed (i.e., stronger winds equate to wider intervals), wind speed can be determined from these intervals. (Obana, 1983).

References:

- Meteorological Satellite Department (1976) Application of Meteorological Satellite Data in Analysis and Forecasting (Translation of ESSA Tech. Rep. NES-51), Japan Meteorological Agency, 105. (In Japanese)
- Obana, R. (1983) Anomalous Clouds under orographical Influence, Analysis and application of Cloud Image from the Meteorological Satellite HIMAWARI, Meteorological Satellite Center, 251-257. (In Japanese)
- Corby, G.A. (1957) A Preliminary Study of Atmospheric Waves using Radiosonde Data, Q.J.R.Met.Soc., 83, 49-60.

6.4.Fog

6.4.1. General Characteristics of Fog

In meteorological satellite observation, it is impossible to tell whether a cloud base is on the ground (i.e., fog) or above it (i.e., cloud) because clouds are seen from outer space. Accordingly, the two phenomena are generally treated together as fog (or St) in cloud analysis using satellite imagery. The related characteristics are described here.

In infrared imagery, fog appears in dark grey. Since its cloud top is low and there is a small temperature difference from surrounding land/sea surfaces, fog identification in such imagery is challenging. The top of fog with a strong surface inversion is warmer than the surrounding fog-free surface. This is known as black fog because it appears darker than the surface.

In visible imagery, fog appears as cloud in light grey. Its top surface is smooth and even, and its top height is nearly uniform. Borders of inland fog areas often follow topography contours, making it easily identifiable in visible imagery (unless covered by thick upper or middle clouds). Fog covered by thin upper clouds can also be identified in most cases, but misidentification as rugged convective clouds may occur when covering granular upper clouds cast shadows over fog. As fog generally moves and transforms slowly, its movement and shape change can be referenced for identification.

As fog is generally less than several hundred meters thick, mountains and hills can act as obstacles and create fog-free areas on their leeward side. Based on this, wind direction can generally be estimated for such locations.

6.4.2. Daytime Fog

Figure 6-4-1 shows B03 visible image with annotation of identified fog areas for 00:00 UTC on 8 March 2016, and Fig. 6-4-2 shows Natural Color RGB composite image for the same time. In these images, veil-like white cloud areas (dashed lines in Fig. 6-4-1), which are lower-cloud with fog, are seen in the Kanto region, the prefectures of Yamanashi and Nagano, and along the coast between Kanto and offshore Sanriku. The phenomenon in northern Kanto and the prefectures of Yamanashi and Nagano is called radiation fog, produced by nighttime radiative cooling, and that along the coast between Kanto and offshore Sanriku is called advection fog, produced by warm and humid inflow. Fog in southern Kanto is a mixture of the radiation and advection types.

Radiation fog in northern Kanto and the prefectures of Yamanashi and Nagano is caused by lower nighttime surface temperatures associated with radiative cooling. It tends to follow topography in valleys and basins, with temporal expansion in the same locations. Fog rapidly dissipates in the morning as a result of solar energy.

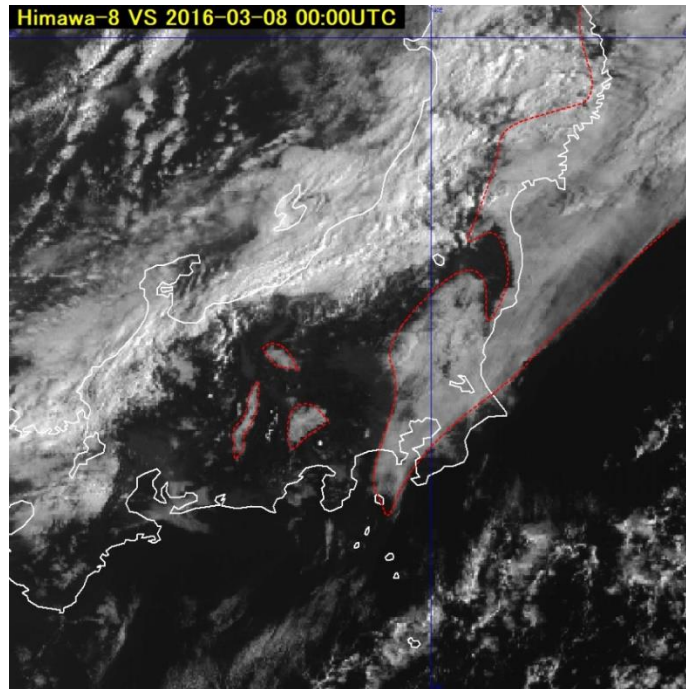


Fig. 6-4-1 B03 visible image with annotations of analyzed fog areas (red broken lines), for 00:00 UTC on 8 March 2016

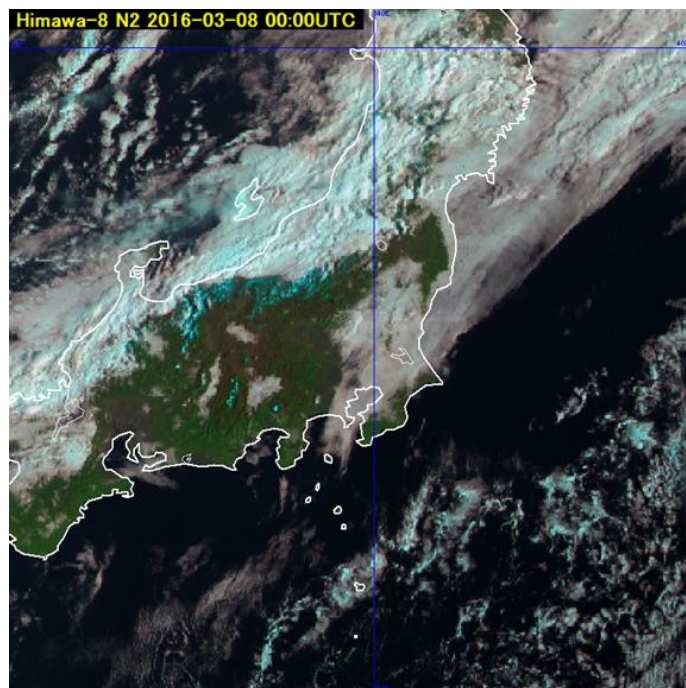


Fig. 6-4-2 Natural Color RGB composite image, at 00:00 UTC on 8 March 2016

However, advection fog over the coast between Kanto and offshore Sanriku does not rapidly dissipate after sunrise. In time-series satellite imagery, shading indicates fog moving northward. The fog in the example referenced here appears to have been caused by an inflow of warm humid air from the southwest onto the cold sea surface, causing saturation and condensation in the lower atmosphere. Figure 6-4-3 shows a surface weather chart for 00:00

UTC on 8 March 2016, Fig. 6-4-4 shows MSM numerical prediction for 925 hPa for wind and temperature, and Fig. 6-4-5 shows sea surface temperature distribution. The fog in the area from the eastern sea off Kanto to offshore Sanriku occurred where warm humid inflow from the southwest overlapped an area with low sea surface temperature.

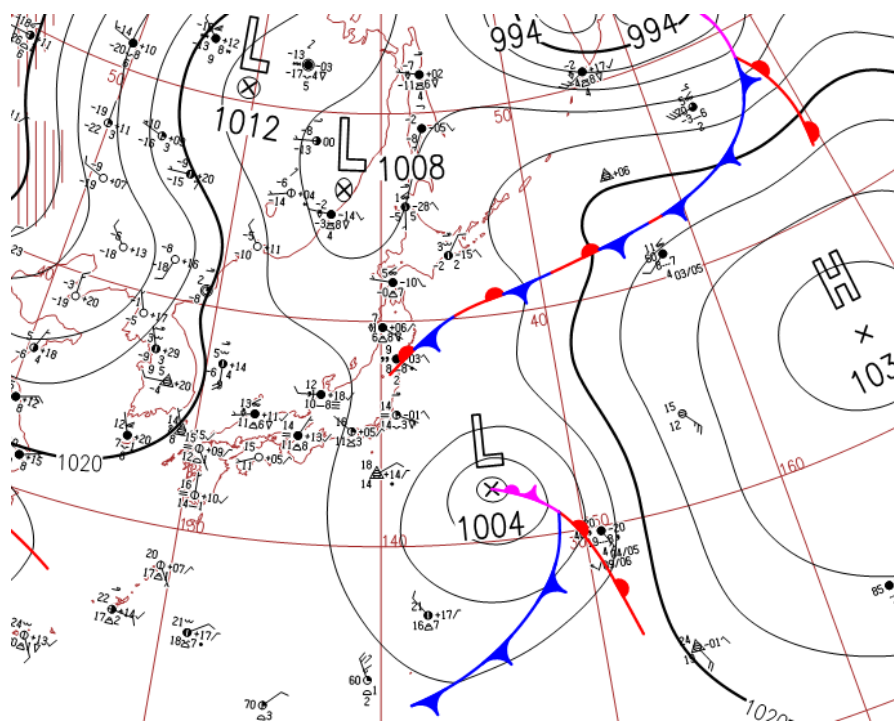


Fig. 6-4-3 Surface weather chart for 00:00 UTC on 8 March 2016

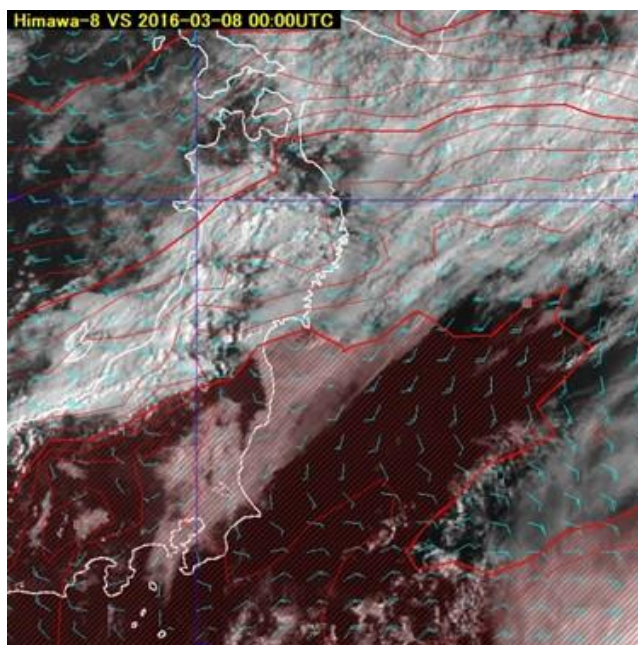


Fig. 6-4-4 B03 visible image and MSM 925 hPa numerical prediction, the area shaded in red indicates temperature above 10 °C

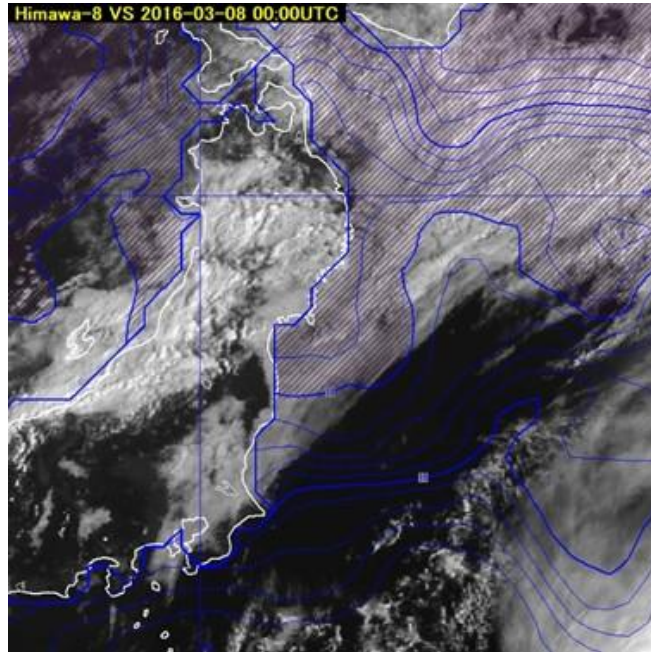


Fig. 6-4-5 B03 visible image and the sea surface temperature, the area shaded in blue indicates temperature below 10 °C

6.4.3. Night Fog

For analysis of nighttime fog, difference images of 3.8 μm (equivalent to B07 for Himawari-8/9) and 10.8 μm (equivalent to B13 for Himawari-8/9) are generally used for Himawari-6 and 7. For Himawari-8/9, Night Microphysics RGB Composite Image provides support for fog detection.

Figure 6-4-6 shows an overlay of difference image for B07 (3.9 μm) and B13 (10.4 μm) for 21:00 UTC on 3 January 2016 and surface weather observation data for the same time. White areas are seen to be scattered over western Japan, and fog was observed in various places from surface weather data.

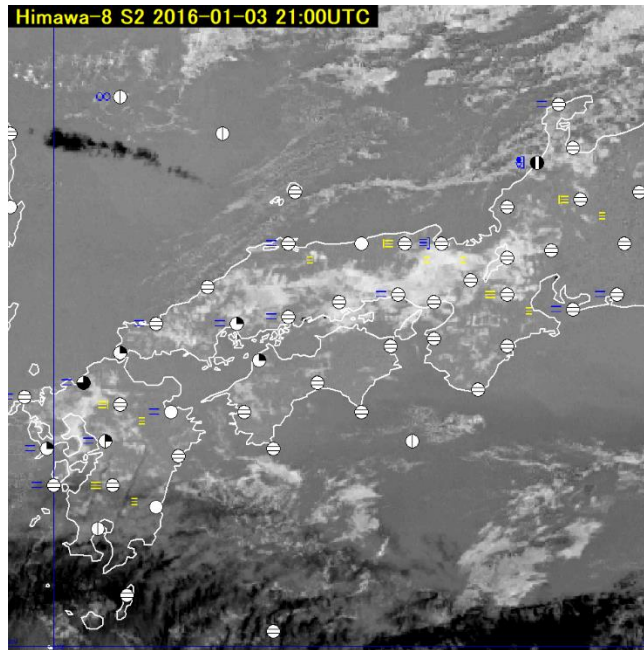


Fig. 6-4-6 The difference image of B07 and B13 of night fog emerged at various locations in western Japan, at 21:00 UTC on 3 January 2016

For comparison, Fig. 6-4-7 shows Night Microphysics RGB composite image for the same time, with pale-green areas making fog easily distinguishable. This image employs difference image of infrared B15 ($12.4\ \mu\text{m}$) and B13 ($10.4\ \mu\text{m}$) and of B13 and B07 ($3.9\ \mu\text{m}$), and B13 infrared image obtained by Himawari-8. It contains more information than difference image for B07 ($3.9\ \mu\text{m}$) and B13 ($10.4\ \mu\text{m}$), making it more useful for monitoring nighttime fog and lower clouds.

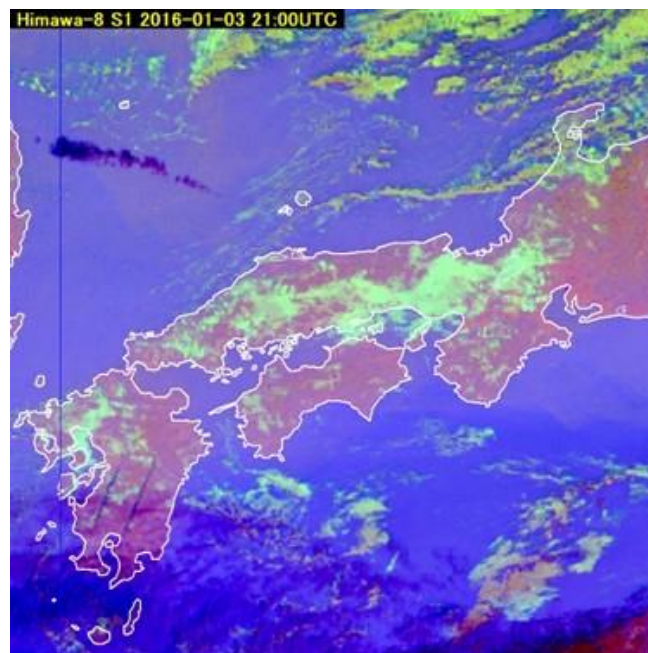


Fig. 6-4-7 Night Microphysics RGB composite image of night fog emerged at various locations

Utilization of Meteorological Satellite Data in Cloud Analysis

in western Japan, at 21:00 UTC on 3 January 2016

6.5. Lower Clouds

6.5.1. General Characteristics of Lower Clouds

In satellite imagery, the term "lower clouds" refers to Cu, Sc and St types as described in Section 2.2. Less is known about lower clouds because they do not cause extreme weather conditions and are difficult to identify from infrared imagery alone (i.e., at nighttime). However, in recent years, more focus has been placed on this cloud type for their usefulness in helping to distinguish between clear and cloudy weather.

Lower clouds appear in grey or white in visible imagery and grey in infrared imagery. Convective lower clouds often form over the sea, and show up in visible imagery as large clusters of tufted or nodular cells. In infrared imagery, they appear as uniform areas with smooth surfaces and indistinct borders for individual cells due to spatial resolution limitations. Over land, stratiform lower clouds often appear as uniform areas with a smooth surface over wide regions in both visible and infrared imagery. Hasegawa (1998) reported that Cu and Sc, which have similar cloud top heights, can be discriminated by noting the faster changes in shape and gradation associated with Cu.

6.5.2. Lower Clouds over the Sea

Figure 6-5-1 presents a B03 visible image of Himawari-8 for 03:00 UTC on 21 January 2016. Lower clouds are observed over the sea, where open- and closed-cell types tend to emerge in winter. Over the sea east of Japan, open-cell Cu and Cg clouds are observed. Closed-cell clouds are also seen over the sea southeast of Hokkaido as a result of convective activity of convective cloud street weakening in correspondence with the cold-air mass. These clouds spread horizontally and changed to Sc type with a more uniform cloud top than Cu and Cg in the open-cell region with an intense cold-air mass.

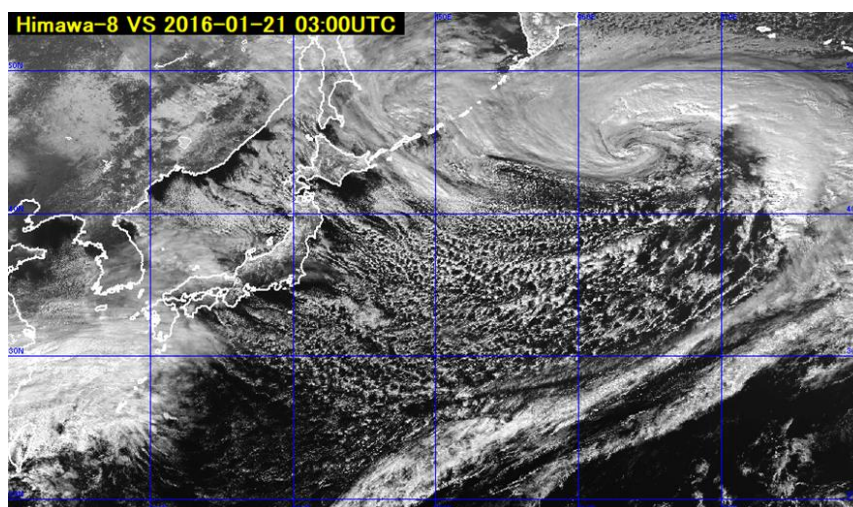


Fig. 6-5-1 B03 visible image for 03:00 UTC on 21 January 2016

6.5.3. Lower Clouds above the China Continent and the South China Sea

Figure 6-5-2 shows B03 visible image and B13 infrared image corresponding to the large-scale lower clouds over the continent and the South China Sea on 20 February 2016. The cloud areas above the continent and the East China Sea were lower St and Sc types. Lower clouds often emerge across wide areas spanning the continent and the East China Sea from winter to spring.

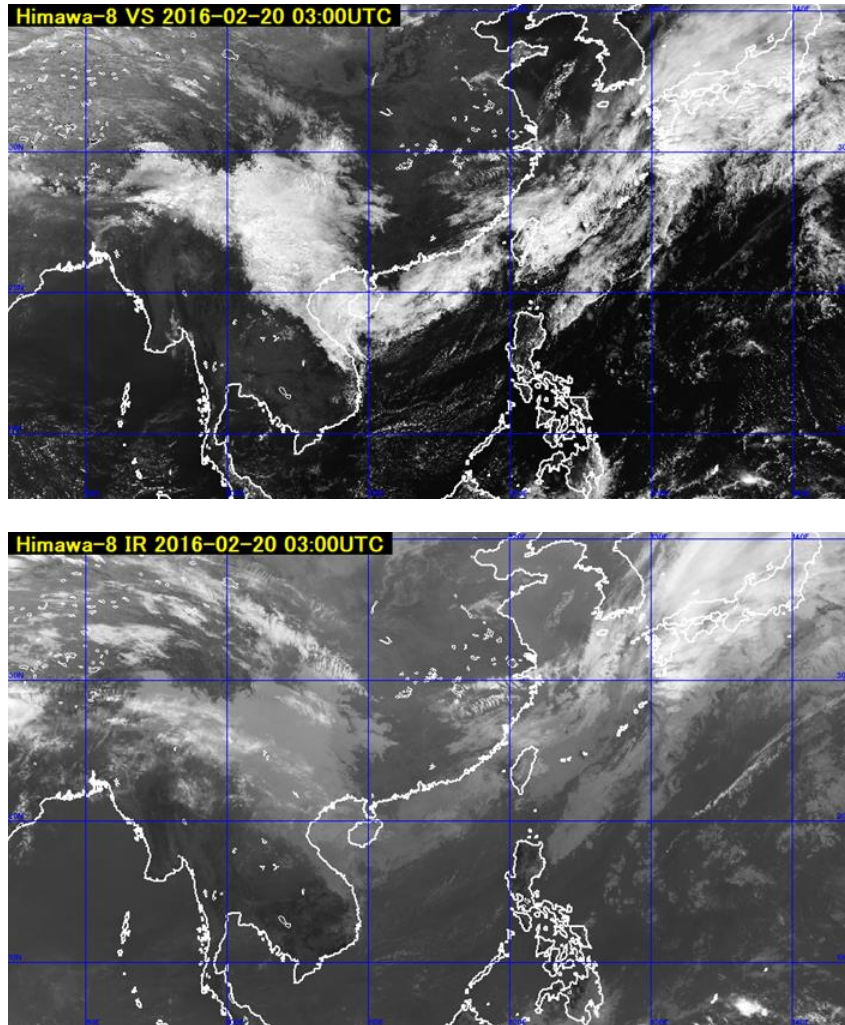


Fig. 6-5-2 B03 visible image (upper) and B13 infrared image (lower) for 03:00 UTC on 20 February 2016

6.5.4. The Distinctive Lower Clouds Seen around Japan

(1) Yamase

Yamase is a cold, wet east or northeast wind that blows over the Pacific coast of northern Japan from early to mid summer. It brings fog and St clouds that block solar radiation and sometimes cause drizzle (Fig. 6-5-3, Bokura, 1995).

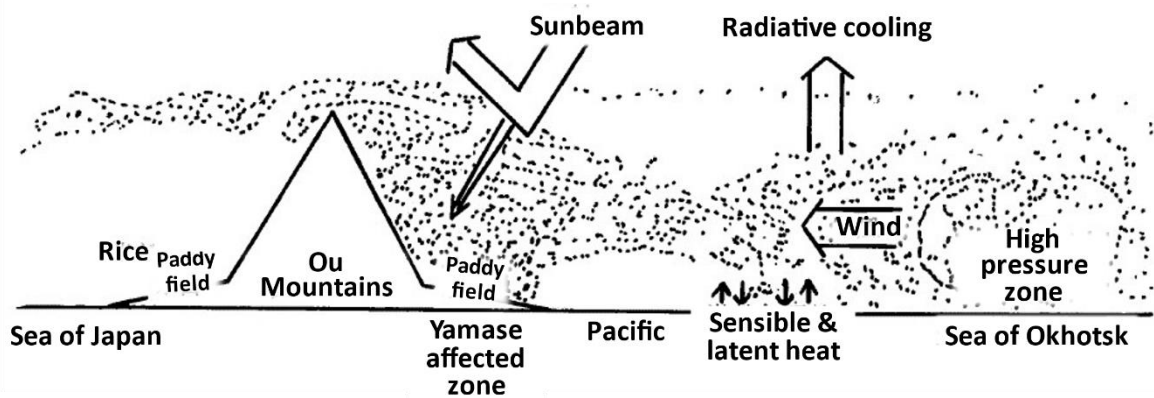


Fig. 6-5-3 Schematic drawing of Yamase (taken from Bokura, 1995)

In satellite imagery, Yamase is recognizable as St or Sc in the area from offshore Sanriku to the Pacific coast of northern and eastern Japan. Figures 6-5-4 and 6-5-5 show accompanying lower clouds. East and northeast winds from the anticyclone above the Sea of Okhotsk cover the southeastern coast of Hokkaido and the Pacific coastline of the Tohoku region with St and Sc. Lower clouds are observed from the Pacific coastlines of the Hokkaido and Tohoku regions to inland areas, while mountains prevent further spreading to the Sea of Japan side. Yamase lower clouds are observed only near the coastline rather than extending over the sea, indicating formation there. In visible imagery, clouds over land are typically brighter than those over sea.

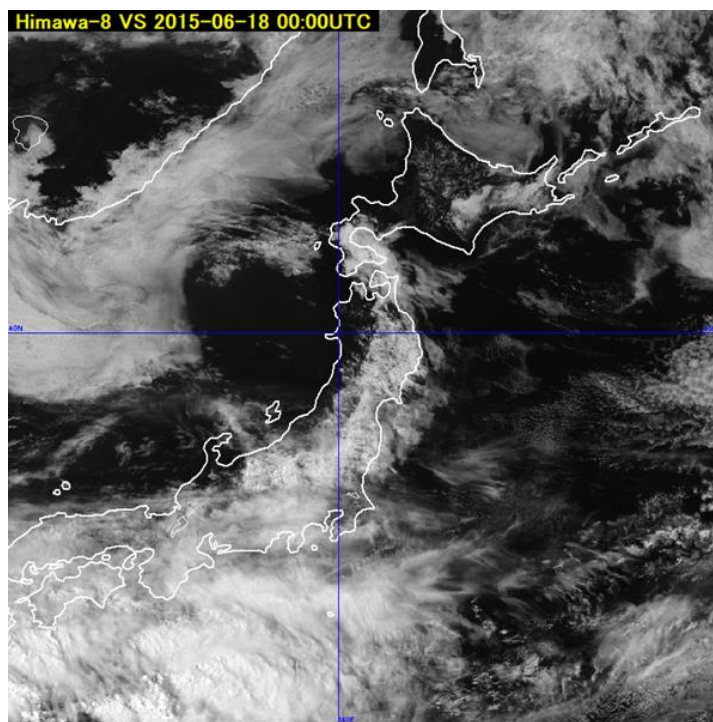


Fig. 6-5-4 B03 visible image for 00:00 UTC on 18 June 2015

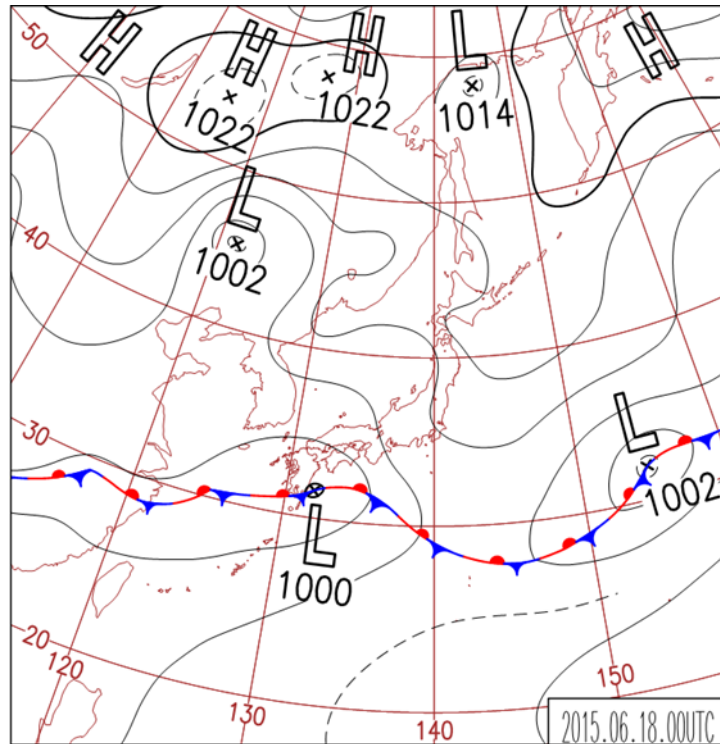


Fig. 6-5-5 Surface weather chart for 00:00 UTC on 18 June 2015

(2) The Lower Clouds along the Shear Line over the Sea South of Kanto

As the winter pressure pattern persists, flow is divided by the mountains in the Chubu region and a shear line forms over the sea south of Kanto with characteristic lower clouds around it. Suzuki and Ando (1992) defined such cloud areas as sea-cucumber or jellyfish types (Fig. 6-5-6). Cloud-area formation is closely associated with shear lines created by two air-current systems coming together around the mountain range of the Chubu region. The lines form over the sea south of Kanto in association with northeastern winds from offshore Kashima via the northern part of the mountain range and western winds from the Enshu Sea via its southern part. Convective clouds emerge along the shear line and expand northward or eastward.

Sea cucumber-type cloud areas consist of convective clouds with a long axis extending zonally along with southward expansion at the southern edge. These tend to move eastward, and have little impact on land. Figure 6-5-7 shows a B03 visible image at 03:00 UTC on 22 February 2016 when a sea cucumber-type cloud area emerged over the sea south and southeast of Kanto, and Fig. 6-5-8 shows a surface weather chart for the same time. A cloud line consisting of Cu stretches east-southeastward along its southern edge, and a cloud area consisting of Sc is seen on its northern side. This type seldom brings extreme weather over land because precipitation is often limited to the Cu line on its southern edge, the western edge of the cloud area often overlaps with the sea south of Kanto, and the air mass moves away from land.

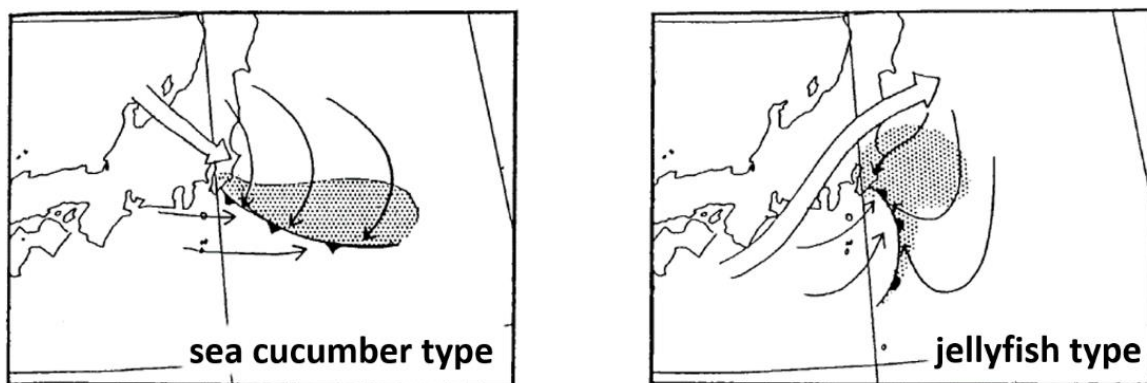


Fig. 6-5-6 Sea cucumber-type and jellyfish-type lower clouds along the shear line over the sea south of Kanto (Suzuki and Ando, 1992). Shaded areas: cloud; thin arrows: surface winds; thick open arrows: winds above the stable layer. Shear lines are indicated with front symbols.

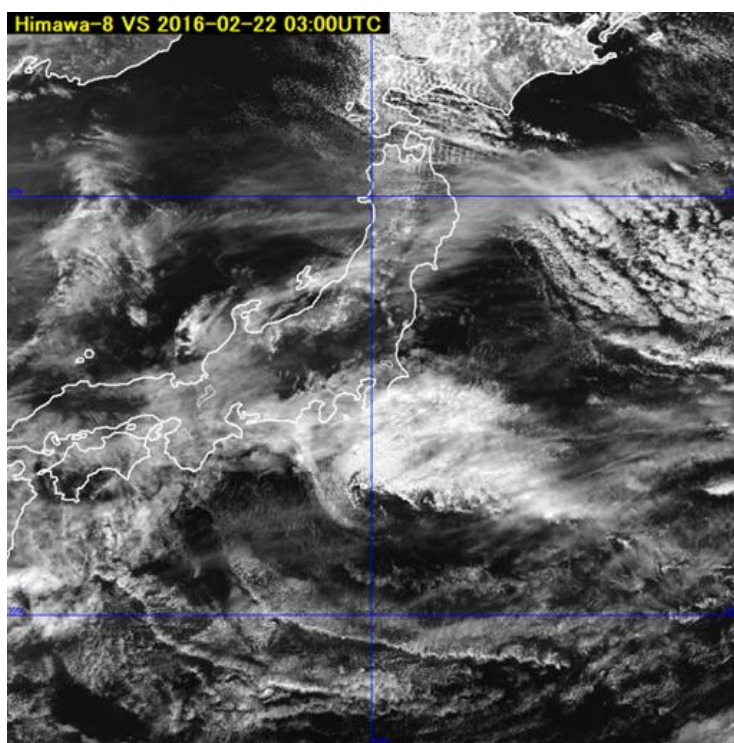


Fig. 6-5-7 B03 visible image for 03:00 UTC on 22 February 2016

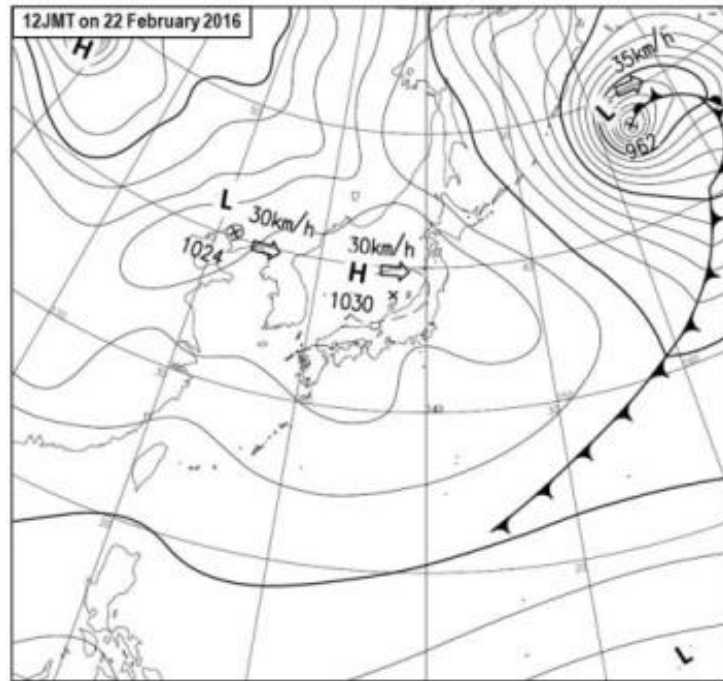


Fig. 6-5-8 Surface weather chart for 03:00 UTC on 22 February 2016

Jellyfish-type cloud areas have a long axis in the meridional direction resembling a comma, with a concave southwest end and a flared north end. These consist of lower clouds, which are often Cu, particularly on the southern and western sides. As the area develops, the northern side is composed of multi-layered clouds covered by upper and middle clouds. These tend to move northward, thereby potentially affecting the Kanto region. Figures 6-5-9 and 6-5-10 show B03 visible imagery for 03:00 UTC on 28 August 2015, when a jellyfish-type cloud area covered the Kanto region, and a surface weather chart for the same time. A Cu cloud line corresponding to a jellyfish arm extended northwest to southeast. A northern cloud area (Cu and Sc) corresponding to the jellyfish body was moving northward and expanding. This type of cloud tends to bring bad weather because precipitation is widely observed throughout its cloud area, it moves toward land, and it may be associated with upper-trough conditions and develop into a cyclone.

Sea cucumber-type cloud areas may transform into jellyfish types with the approach of an upper trough (there is no reverse transformation). Accordingly, observation of pattern developments in satellite imagery is important for forecasting.

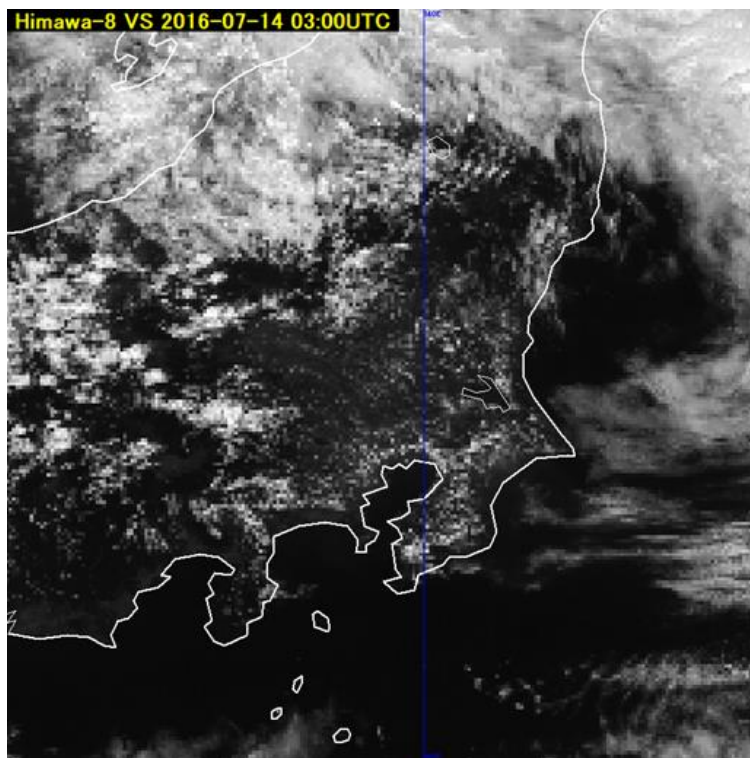


Fig. 6-5-9 B03 visible image for 03:00 UTC on 28 August 2015

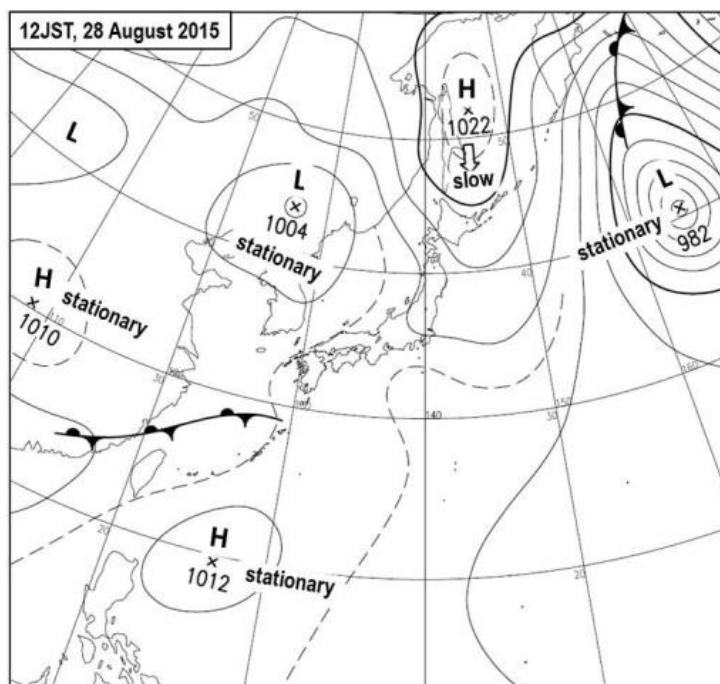


Fig. 6-5-10 Surface weather chart for 03:00 UTC on 28 August 2015

(3) Sea Breeze Front

Focus here is placed on a local-scale front that occurs at the tip of a summer sea breeze. Figure 6-5-11 shows B03 visible image, Fig. 6-5-12 shows True Color Reproduction image with prominent small Cu clouds for 03:00 UTC on 14 July 2016, and Fig. 6-5-13 shows a surface weather chart for the same time. Figure 6-5-12 clearly shows a Cu cloud line with a shape

along the coast near the tip of the sea breeze slightly inland from the coast of the Kanto region.

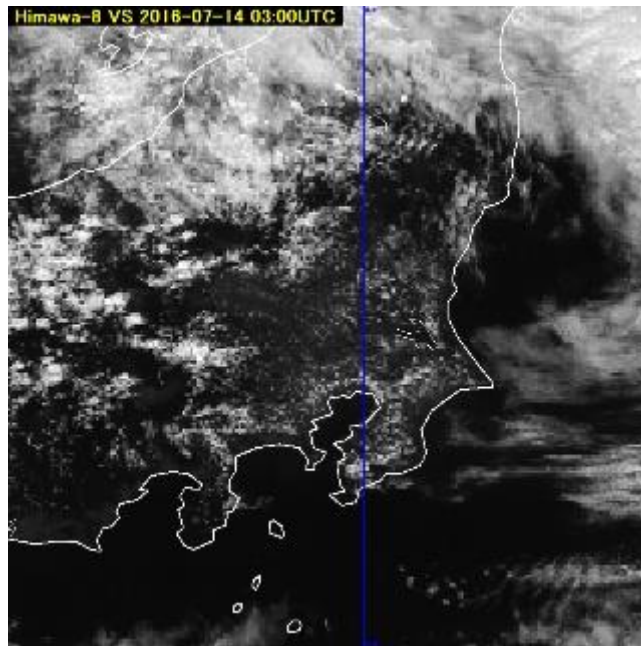


Fig. 6-5-11 B03 visible image for 03:00 UTC on 14 July 2016

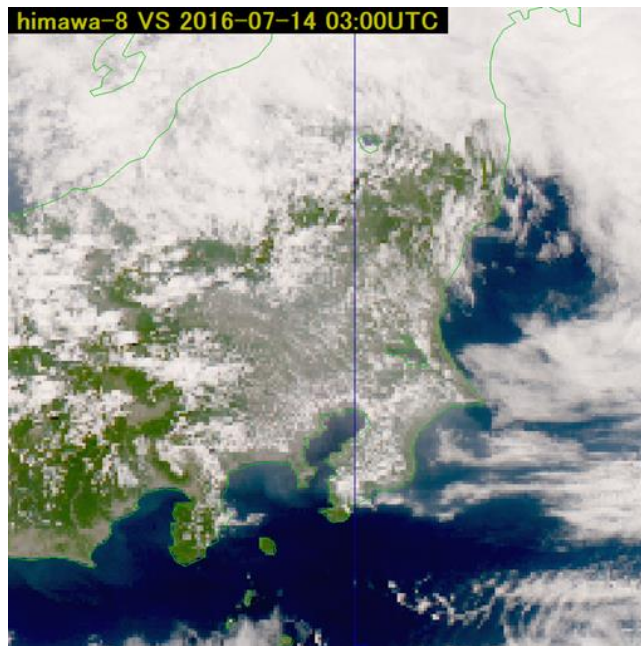


Fig. 6-5-12 True Color Reproduction image for 03:00 UTC on 14 July 2016

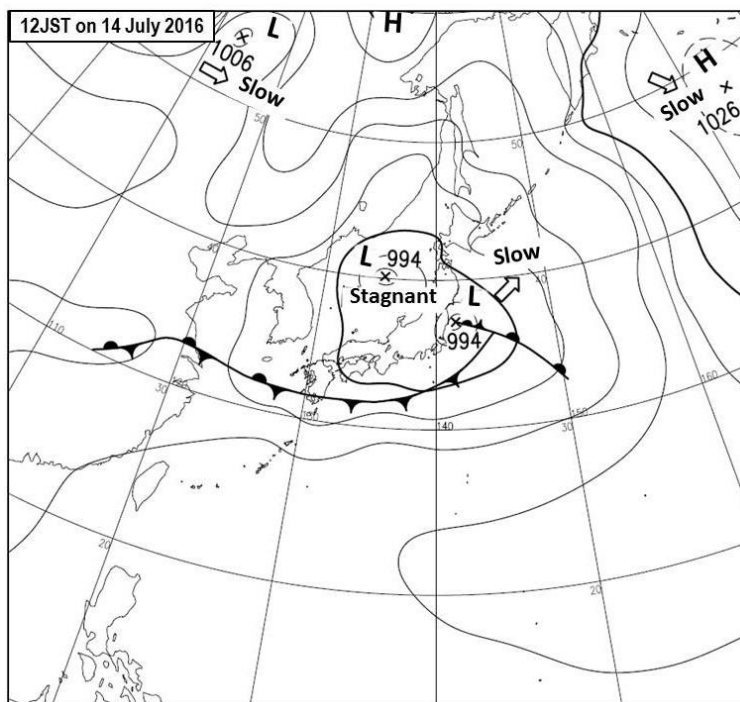


Fig. 6-5-13 Surface weather chart for 03:00 UTC on 14 July 2016

(4) Barrage Cloud Associated with Foehn

Moist air masses rising along mountain slopes become saturated, and clouds form on the windward side of the mountain. When the masses blow down on the leeward side, they dry due to adiabatic warming, and cloud dissipates (Fig. 6-5-14) in a phenomenon known as foehn. In satellite imagery, clouds appear on the windward side, and weather is fair on the leeward side. Low clouds on the windward side associated with foehn are called barrage cloud (Bader *et al.*, 1995). Figures 6-5-15 and 6-5-16 show B03 visible image and Natural Color RGB composite image for 00:00 UTC on 13 April 2016 when foehn was prominent in Toyama Prefecture. Figure 6-5-17 shows a surface weather chart for the same time.

Figures 6-5-15 and 6-5-16 show lower clouds on the Pacific side from the Kinki region to the Kanto region. These were blocked by high mountains in the Chubu region. In Fig. 6-5-16 (Natural Color RGB composite image), barrage clouds appear light blue, indicating domination by water clouds.

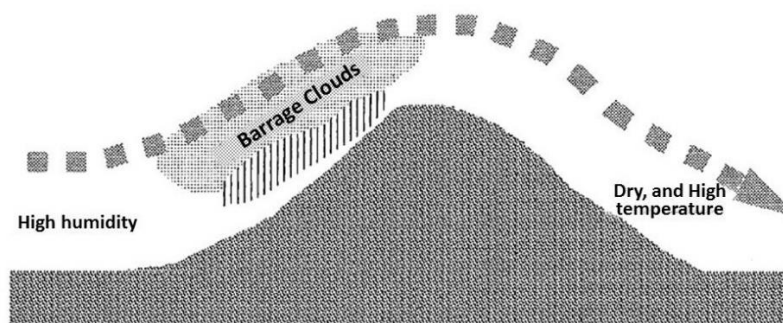


Fig. 6-5-14 Schematic diagram of foehn

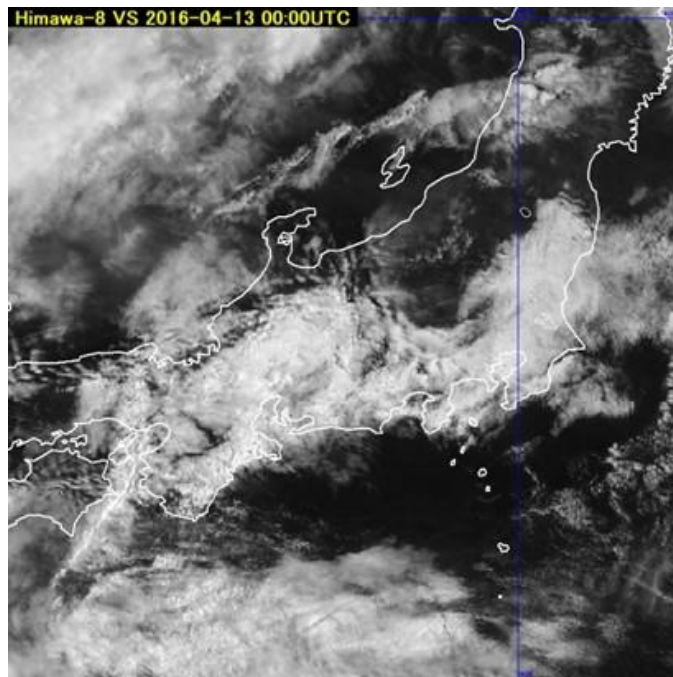


Fig. 6-5-15 B03 visible image for 00:00 UTC on 13 April 2016

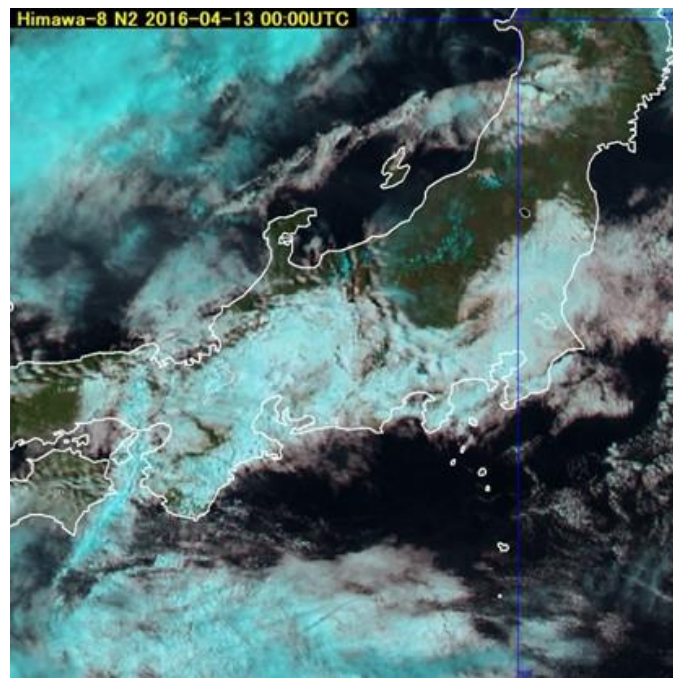


Fig. 6-5-16 Natural Color RGB composite image for 00:00 UTC on 13 April 2016

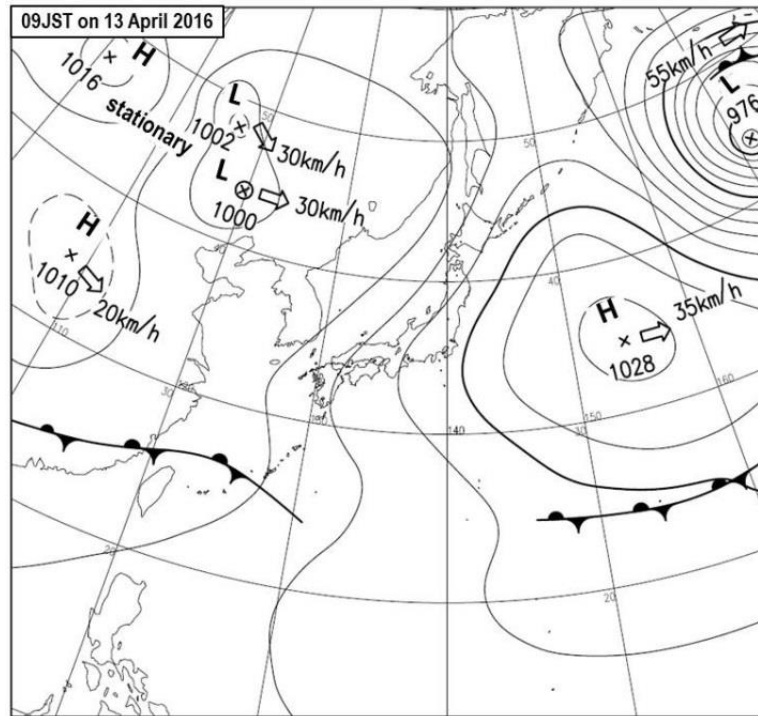


Fig. 6-5-17 Surface weather chart for 00:00 UTC on 13 April 2016

References:

- Hasegawa, Y. (1998) Features of Low Cloud and Fog on Satellite Image, Nephanalysis Case Study Reports, Meteorological Satellite Center, 1-5.
- Bokura, K. (1995) "Yamase" and Cold Summer Damage, Kisyo-kenkyu Note, 183, 15-30.
- Suzuki, K. and Y. Ando (1992) A Conceptual Model of Meso- α Scale Cloud System that Brings Local Cloudy Weather around Kanto Area, Journal of Meteorological Research, 44, 63-79.
- Bader, M. J., G. S. Forbes, J. R. Grant, R. B. E. Lilley and A. J. Waters (1995) Images in weather forecasting, Cambridge Univ. Press, 499pp.